Republic of Iraq
Ministry of Higher Education and Scientific Research
University of Babylon / College of Sciences
Department of Physics

# Study of Some Physical Properties of p-$Mg_xZnO_{1-x}$/n-Si Photodetector and Gas Sensor

A thesis
Submitted to the Council of College of Sciences, University of Babylon in Partial Fulfillment of the Requirements of the Degree of Doctors of Philosophy in Physics

By

**Saleem Hamza Trier Jabber**

B. Sc. in Physics/ 1999
M.Sc. in Physics/ 2006

Supervised by

**Prof. Dr.**

**Abdulazeez O. Mousa Al-Ogaili**

2017 A.D. 1438 A.H.

جمهورية العراق
وزارة التعليم العالي والبحث العلمي
جامعة بابل/ كلية العلوم
قسم الفيزياء

# دراسة بعض الخصائص الفيزيائية $p\text{-}Mg_xZnO_{1-x}/n\text{-}Si$ للكاشف الضوئي والمتحسس الغازي

رسالة مقدمة إلى
مجلس كلية العلوم في جامعة بابل كجزء من متطلبات
نيل درجة دكتوراه فلسفة في الفيزياء
تقدم بها

**سليم حمزة طرير جبر**

بكالوريوس فيزياء/ ١٩٩٩

ماجستير فيزياء / ٢٠٠٦

بإشراف
الاستاذ الدكتور

**عبد العزيز عبيد موسى العكيلي**

٢٠١٧ م ١٤٣٨هـ

بِسْمِ اللّهِ الرَّحْمَنِ الرَّحِيمِ

إِنَّا فَتَحْنَا لَكَ فَتْحًا مُّبِينًا ﴿١﴾ لِيَغْفِرَ لَكَ اللَّهُ مَا تَقَدَّمَ مِن ذَنبِكَ وَمَا تَأَخَّرَ وَيُتِمَّ نِعْمَتَهُ عَلَيْكَ وَيَهْدِيَكَ صِرَاطًا مُّسْتَقِيمًا ﴿٢﴾ وَيَنصُرَكَ اللَّهُ نَصْرًا عَزِيزًا ﴿٣﴾

صَدَق اللَّه الْعَلِيُّ الْعَظِيْم

سورة الفتح آية (١–٣)

## *Dedication*

*To Allah who created me and in the way of Allah.*

*To the best of Allah creation Mohammad Al-Mustafa (Allah Blessing and Peace be upon him) and the Infallible Imams, (peace be upon them)*

*To Imam Mahdi (Allah hasten his reappearance).*

*To who recounted to the land of their blood  the martyrs of Iraq .*

*To all who helped me  even if for word.*

*To all my professors distinguished.*

*To all of my friends.*

*To my family.*

*Dedicate this humble effort.*

*Saleem*

# *Acknowledgments*

*I should thank my Almighty (Allah) for helping me in completing my thesis.*

*I would like to express my deep thanks and gratitude to my supervisor,* ***Prof.Dr. Abdulazeez O. Mousa Al-Ogaili*** *for his suggestion the subject of my research and remarkable notes during the whole work of mine.*

*Many thanks to the deanery of the College of Sciences in Babylon University and the Department of Physics for offering me the opportunity to complete my thesis.*

*I would like to thank* ***Dr. Noor Amer Abokhumra*** *to help me through the practical period.*

*I would like to thank* ***Dr. Mohammad Hadi Al-shimmery****, College of Basic Education, the University of Babylon to help me to complete some tests.*

*My great thanks are expressed to all my friends.*

*Saleem*

## Supervisor Certification

I certify that this thesis titled "**Study of Some Physical Properties of $p\text{-}Mg_xZnO_{1-x}/n\text{-}Si$ Photodetector and Gas Sensor**" was prepared by "**Saleem Hamza Trier Jabber**" under my supervision at Department of Physics, College of Sciences, University of Babylon, as a partial fulfillment of the requirements for the degree of doctor philosophy of science in physics, specialization in the solid state physics.

Signature:

Supervisor: **Dr. Abdulazeez O. Mousa Al-Ogaili**

Title : **Professor**

Address : **University of Babylon - College of Sciences**

**Department of Physics**

Date : / / **2017**

## Certification of the Head of the Department

In view of the available recommendation, I forward this dissertation for debate by the examination committee.

Signature:

Advisor : **Dr. Khalid Hussain Hatif**

Title : **Professor**

Address : **Head of Department of Physics - College of Sciences**

**University of Babylon**

Date : / / **2017**

We certify that we have read this thesis, entitled "**Study of Some Physical Properties of $p\text{-}Mg_xZnO_{1-x}/n\text{-}Si$ Photodetector and Gas Sensor** " and as

examination committee, we examined the student "**Saleem Hamza Trier Jabber**" on its contents, and that in our opinion it is adequate for the partial fulfillment of requirements for the degree of doctor of philosophy of sciences in physics, the specialization of the solid state physics.

Signature :
Name : Dr. Sahib N. Abdul Wahid
Title : Professor
Address : University of Kufa / College of Education for Women /Dep. of Phy.
Date : / / 2017
(Member)

Signature:
Name : Dr. Raheem G. Kadhim
Title : Professor
Address : University of Babylon / College of Sciences / Dep. of Physics
Date : / / 2017
(Chairman)

Signature:
Name : Dr. Majeed A. Habeeb
Title : Assist Professor
Address : University of Babylon/ College of Education for Pure Sci. /Dep. of Phy.
Date : / / 2017
(Member)

Signature :
Name : Dr. Hayfa G. Rashid
Title : Professor
Address : Al-Mustansiriyah University / College of Education / Dep. of Phy.
Date : / / 2017
(Member)

Signature:
Name : Dr. Abdulazeez O. Mousa Al-Ogaili
Title Title : P
Address : University of Babylon/ College of Sciences / Dep. of Physics
Date : / / 2017
(Member and Supervisor )

Signature:
Name : Dr. Abbas J. Lafta
Title : Assist Professor
Address : University of Babylon / College of Sciences / Dep. of Chemistry
Date : / / 2017
(Member)

**Approved by the College Committee on Graduate Studies :**

Signature:
Name : Dr. Haider Kamil Zaidan
Title : Professor
Address : Dean of the College of Sciences - University of Babylon
Date : / / 2017

**Summary**

In this work $Mg_xZnO_{1-x}$ thin films have been prepared using a chemical spraying pyrolysis (CSP) technique which is an easy and suitable way of deposition over large areas. Mixed solutions have been growth at different volumetric percentages (0, 30, 50, 70, and 90)% and deposited on glass and silicon substrates at temperatures (400,450, and 500) °C. The thickness was installed by installing the number of sprays. The thickness of all the films were (80 ±5) nm, have been using nitrogen gas. The crystal structure was examined by using X-ray diffraction (XRD) technique. The results showed that all the prepared were polycrystalline films, showing improvement in the crystal structure by change at temperature.

Topography of the surface of the prepared films have been studied by using atomic force microscope (AFM), field emission scanning electron microscopy (FESEM), and energy dispersive X-ray spectroscopy (EDX). The increase in the percent of Mg-content in the films lead to decrease in surface roughness. (EDX) showed that films contain elements (Si, N, O, Zn, and Mg) as expected. Raman scattering have been measured for $Mg_xZnO_{1-x}$/n-Si thin films at different Mg-content. It exhibits two intense bands at (601 and 1202) $cm^{-1}$, corresponding to the $E_2^{high}$ first-order Raman modes, and second-order mode the $A_1$(LO) first-order mode of ZnO. As it increases Mg-content up to (50)%,the $E_2^{high}$ mode the decrease in intensity.

The optical properties of the films prepared by the optical transmittance measurements in the spectral region (300-700) nm. The results of the transmittance rang from (65-89)% when increasing the Mg-content from (30 to 90)% at substrate temperature of (400)°C and increased transmittance more when increase the temperature to become (84-95)% at the same Mg-content, which makes it suitable for applications gas sensors. Absorbance and reflectivity have been measured which were decreases by increasing temperatures. Absorption coefficient was measured for all the films, and its value more than ($10^4$) $cm^{-1}$.

Direct energy gap was calculated for pure ZnO was (3.18 and 3.21 and 3.19) eV and the corresponding to substrate temperatures (400,450, and 500) °C respectively.

The optical constants such as refractive index, extinction coefficient and dielectric constant have been calculated for all preparing films. The optical energy gap was calculated by photoluminescence spectrometer were few sensitive between (3.558 - 3.531) eV.

The electrical properties such as D.C electrical conductivity and Hall effect have been studied, results showed measurements Hall that the pure ZnO film was negative type (n-type), while $Mg_xZnO_{1-x}$ films were (p-type), and have two activation energies ($Ea_1$,and $Ea_2$). Capacity of $Mg_xZnO_{1-x}$/n-Si photodetector have been measured as a function of voltage reverse bias at frequency ranges (0.6-1) MHz. These results indicated that the photodetector is abrupt type. It was found that the value of built-in potential, decreases with increasing Mg-content and increases when Mg- content ratio (90%). The current-voltage characteristics of the $Mg_xZnO_{1-x}$/n-Si under dark conditions showed that forward bias current varied exponentially with voltage bias. The ideality factor and current saturation decreased with increasing Mg-content in the films whereas increased at high temperatures has been noticed.

In this work the study of the spectral characteristics of the photodetector $Mg_xZnO_{1-x}$/n-Si and found that the spectral response values, quantum efficiency and specific detectivity increased with increasing Mg-content ratios, while the noise equivalent power (NEP) decrease when the Mg-content is increased.

The beaks response appear at (450)nm equal to (13.51) A/W, and (900) nm equal to (36.83)A/W. It has been found that the gain for the $Mg_xZnO_{1-x}$/n-Si increases with increasing temperatures. The sensitivity of the $Mg_xZnO_{1-x}$/ n-Si to ($NO_2$) gas in air a All samples were tested at ambient has been measured in the gas sensing system. and 6V bias voltage. The best ratio dopant of the Mg-content is ratio 3% $NO_2$:air ) $^oC$ of the ٤٠٠x=(5)%, (200)$^oC$ operating temperature, and substrate temperature ( silicon substrate. The maximum sensitivity is (90.80) % , fast response time is (15.3s) and recovery time is (42.3s).

## Contents

| Title | Page |
| --- | --- |

| | |
|---|---|
| Contents | I |
| List of Symbols and Abbreviations | VII |
| List of Figures | XIV |
| List of Tables | XVIII |
| Summary | XX |

| No. | Subject | Page No. |
|---|---|---|
| | **CHAPTER ONE: INTRODUCTION** | **(1-20)** |
| 1.1 | Introduction | 1 |
| 1.2 | Crystal Structure of ZnO | 2 |
| 1.2.1 | Basic Crystal Structures of ZnO | ٤ |
| 1.2.2 | Applications of ZnO | 5 |
| 1.3 | Magnesium Oxide Thin Film, its Applications | 6 |
| 1.4 | The p-$Mg_xZnO_{1-x}$ Thin Films | 8 |
| 1.5 | Crystallite Silicon | 9 |
| 1.6 | Methods of Preparing Thin Films | 11 |
| 1.6.1 | Chemical Spray Pyrolysis Technique | 12 |
| 1.6.2 | Advantages of Spray Pyrolysis Technique | 12 |
| 1.7 | Literature Survey | 13 |
| 1.8 | Aims of the Work | 20 |
| | **CHAPTER TWO: THEORETICAL CONSIDERATION** | **(21-53)** |
| 2.1 | Introduction | 21 |
| 2.2 | X-Ray Diffraction | 21 |
| 2.2.1 | Lattice Constants | 21 |
| 2.2.2 | Full Width at Half Maximum | 22 |
| 2.2.3 | Average Crystallite Size | 22 |
| 2.2.4 | Microstrains | 22 |

| No. | Subject | Page No. |
|---|---|---|
| 2.2.5 | Dislocation Density | 23 |
| 2.2.6 | Number of Layers | 23 |
| 2.3 | Field Emission Scanning Electron Microscopy | 23 |
| 2.4 | Atomic Force Microscopy | 24 |
| 2.5 | Raman Spectroscopy | 24 |
| 2.5.1 | Raman Spectroscopy of ZnO Thin Films | 27 |
| 2.5.2 | Impurities and Defects | 28 |
| 2.6 | Optical Properties | 28 |
| 2.6.1 | Optical Absorption and Absorption Edge | 28 |
| 2.6.2 | Direct Transitions | 29 |
| 2.6.3 | Optical Constants | 30 |
| 2.7 | Electrical Properties of ZnO Thin Films | 31 |
| 2.7.1 | The Direct Continuous Electrical Conductivity | 32 |
| 2.7.2 | Hall Effect | 33 |
| 2.8 | Theory of Heterojunction | 35 |
| 2.8.1 | Band Profile of Heterojunction | 36 |
| 2.8.2 | Lattice Mismatch | 36 |
| 2.8.3 | Thermal Mismatch | 37 |
| 2.8.4 | Interdiffusion | 37 |
| 2.8.5 | Electrical Properties of Heterojuncton | 37 |
| ١8.5.٢, | Capacitance -Voltage Characteristics | 38 |
| 2.8.5.2 | Dark Current-Voltage Characteristics | 38 |
| 2.8.5.3 | Under Illumination Current–Voltage Characteristics | 39 |
| 2.9 | Photocurrent Gain | 40 |
| 2.10 | Photon Detectors | 40 |
| 2.10.1 | Photoconductive Detectors | 41 |
| 2.10.1.1 | The Intrinsic Photoconductive Type | 42 |

| No. | Subject | Page No. |
| --- | --- | --- |
| 2.10.1.2 | The Extrinsic Photoconductive Type | 42 |
| 2.11 | The Figure of Merit | 44 |
| 2.11.1 | The Responsivity | 44 |
| 2.11.2 | The Quantum Efficiency | 44 |
| 2.11.3 | The Noise in Detectors | 44 |
| 2.11.4 | Detectivity and Specific Detectivity | 45 |
| 2.11.5 | Noise Equivalent Power | 45 |
| 2.12 | ZnO and its Dopant Gas Sensors | 46 |
| 2.12.1 | Thin Film Sensor | 46 |
| 2.12.2 | Thin Film Resistive of Gas Sensors | 47 |
| 2.13 | Sensing Properties | 47 |
| 2.13.1 | Gas and Chemical Sensing | 48 |
| 2.13.2 | Chemical Sensors | 48 |
| 2.14 | Gas Sensing Properties | 50 |
| 2.14.1 | The Sensitivity | 51 |
| 2.14.2 | The Selectivity | 52 |
|  | **CHAPTER THREE: EXPERIMENTAL DETAILS** | **(53-66)** |
| 3.1 | Introduction | 53 |
| 3.2 | Preparation of $Mg_xZnO_{1-x}$ Thin Films | 55 |
| 3.2.1 | Experimental Set-up of (CSP) | 55 |
| 3.2.2 | Preparing of Substrates | 56 |
| 3.2.2.1 | Glass Substrate | 56 |
| 3.2.2.2 | Silicon Substrate | 57 |
| 3.2.3 | Preparation of the Spray Solutions | 57 |
| 3.2.4 | Masks and Ohmic Contact | 58 |
| 3.3 | Structural and Morphological Measurements | 58 |
| 3.3.1 | X-Ray Diffraction | 58 |

| No. | Subject | Page No. |
|---|---|---|
| ٣,٣,٢ | Field Emission Scanning Electron Microscopy | 59 |
| 3.3.3 | Atomic Force Microscope | 59 |
| ٣,٣,٤ | Raman Shift Measurements | 60 |
| ٣,٣,٥ | Film Thickness Measurements | 61 |
| ٣,٤ | Optical Properties Measurements | 61 |
| ٣,٤,١ | UV-Vis Measurements | 61 |
| 3.4.2 | Photoluminescence Measurements | 62 |
| 3.5 | Electrical Measurements | 62 |
| ٣,٥,١ | The Direct Continuous Conductivity Measurements | 62 |
| ٣,٥,٢ | Hall Effect Measurements | 62 |
| 3.5.3 | The Photodetector Al/ $Mg_xZnO_{1-x}$/n-Si/Al Characterization | 62 |
| 3.5.3.1 | Capacitance -Voltage Measurements | 62 |
| ٣,٥,٣,٢ | Dark and Illumination for Current-Voltage Measurements | 63 |
| ٣,٦ | Figure of Merit of $Mg_xZnO_{1-x}$ /n-Si Photodetector | 63 |
| 3.7 | Gas Sensor System | 63 |
| 3.8 | Al-Interdigitated Electrodes | 64 |
| 3.9 | Sensor Testing Procedure | 65 |
| | **CHAPTER FOUR : RESULTS AND DISCUSSION** | **(67-147)** |
| 4.1 | Introduction | 67 |
| 4.2 | Structure and Surface Morphology for $Mg_xZnO_{1-x}$ Thin Films | 67 |
| 4.2.1 | X-Ray Diffraction Analysis | 67 |
| 4.2.2 | Lattice Constants (a ,and c) | 78 |
| 4.2.3 | Full Width at Half Maximum | 79 |
| 4.2.4 | Average Crystallite Size | 80 |
| 4.2.5 | Microstrains | 80 |
| 4.2.6 | Dislocation Density | 80 |
| 4.3 | Atomic Force Microscope | 81 |

| No. | Subject | Page No. |
|---|---|---|
| 4.4 | Optical Properties of the $Mg_xZnO_{x-1}$ Thin Films | 88 |
| 4.4.1 | Measurements of Transmission Spectrum for $Mg_xZnO_{1-x}$ Thin Films | 88 |
| 4.4.2 | Measurements of Absorbance Spectrum for $Mg_xZnO_{1-x}$ Thin Films | 90 |
| 4.4.3 | Measurements of Reflectance Spectrum for $Mg_xZnO_{1-x}$ Thin Films | 92 |
| 4.4.4 | Measurements of Absorption Coefficients for $Mg_xZnO_{1-x}$ Thin Films | 94 |
| 4.4.5 | Measurements of Optical Energy Gap for $Mg_xZnO_{1-x}$ Thin Films | 95 |
| 4.4.6 | Measurements of Refractive Index for $Mg_xZnO_{1-x}$ Thin Films | 99 |
| 4.4.7 | Measurements of Extinction Coefficient for $Mg_xZnO_{1-x}$ Thin Films | 100 |
| 4.4.8 | Measurements of Real and Imaginary Dielectric Constant for $Mg_xZnO_{1-x}$ Thin Films | 101 |
| 4.5 | Photoluminescence for $Mg_xZnO_{1-x}$ Investigation Temperatures | 102 |
| 4.6 | Electrical Properties of ZnO, and $Mg_xZnO_{1-x}$ Thin Films | 106 |
| 4.6.1 | Direct Continuous Electrical Conductivity of ZnO, and $Mg_xZnO_{1-x}$ Thin Films | 106 |
| 4.6.2 | The Activation Energy of ZnO, and $Mg_xZnO_{1-x}$ Thin Films | 106 |
| 4.6.3 | Hall Effect Measurements of ZnO, and $Mg_xZnO_{1-x}$ Thin Films | 110 |
| 4.7 | Characterization of ZnO/n-Si, and $Mg_xZnO_{1-x}$/n-Si Photodetector | 111 |
| 4.7.1 | Surface Morphology Properties of ZnO/n-Si, and $Mg_xZnO_{1-x}$/n-Si Photodetector | 112 |
| 4.7.1.1 | Field Emission Scanning Electron Microscopy for $Mg_xZnO_{1-x}$/n-Si Photodetector | 112 |
| 4.7.1.2 | Elemental Analysis for $Mg_xZnO_{1-x}$/n-Si Photodetector | 117 |
| 4.7.2 | Optical Properties for $Mg_xZnO_{1-x}$/n-Si Photodetector | 117 |
| 4.7.2.1 | Photoluminescence for $Mg_xZnO_{1-x}$/n-Si Photodetector | 118 |
| 4.8 | Raman Shift for $Mg_xZnO_{1-x}$/n-Si at Substrate Temperatures (400,450,and 500) $^oC$ | 120 |
| 4.9 | Electrical and Photoconductive Properties for Al/$Mg_xZnO_{1-x}$/n-Si/Al Photodetector | 124 |
| 4.9.1 | C-V Characteristic of Al/$Mg_xZnO_{1-x}$/n-Si/Al Photodetector | 124 |

| No. | Subject | Page No. |
|---|---|---|
| 4.9.2 | I-V Characteristics for $Mg_xZnO_{1-x}$ /n-Si Photodetector under Dark | 129 |
| 4.9.3 | I-V Characteristics for $Mg_xZnO_{1-x}$ /n-Si Photodetector under Illumination | 132 |
| 4.9.4 | Gain for $Mg_xZnO_{1-x}$/n-Si Photodetector | 134 |
| 4.10 | Figures of Merit for $Mg_xZnO_{1-x}$ /n-Si Photoconductive Detectors | 136 |
| 4.10.1 | The Spectral Responsivity | 136 |
| 4.10.2 | The Quantum Efficiency | 138 |
| 4.10.3 | The Specific Detectivity | 139 |
| 4.10.4 | Noise Equivalent Power | 140 |
| 4.11 | Gas Sensing Measurements | 141 |
| 4.11.1 | Determination of Operation Temperature of $Mg_xZnO_{1-x}$ /n-Si Sensor | 141 |
| 4.11.2 | Response and Recovery Time of $Mg_xZnO_{1-x}$/n-Si Sensor | 142 |
| 4.12 | Conclusions | 145 |
| 4.13 | Future Works | 146 |
| | References | 148 |


## List of Symbols and Abbreviations

| Symbol | Description | Unit |
|---|---|---|
| A | Absorbance | |
| $A_r$ | Cross Section Area of the Film | $cm^2$ |
| $\bar{A}$ | Area of the Sensor | $cm^2$ |
| $A^*$ | Effective Richardson Constant | |

| | | |
|---|---|---|
| AE | Arc Evaporation | |
| AFM | Atomic Force Microscopy | |
| ALD | Atomic Layer Deposition Technique | |
| APCVD | Atmospheric Pressure Chemical Vapor Deposition | |
| ASTM | American Standard for Testing Material | |
| $B_Z$ | Magnetic Field | $W_b/cm^2$ |
| c | Light Velocity | m/s |
| C | Capacitance | $F/cm^2$ |
| C.B | Conduction Band | |
| $C_{6V}$ | Symmetry of Wurtzite Structure for ZnO | |
| CM | Chemical Methods | |
| CS | Cathode Sputtering | |
| c-Si | Crystallite Silicon | |
| CSP | Chemical Spry Pyrolysis | |
| C-V | Capacitance-Voltage | |
| D | Detectivity | |
| D* | Specific Detectivity | |
| DCS | Direct Current Sputtering | |
| $d_{hkl}$ | Spacing between Diffracting Planes | nm |
| DLEs | Deep Level Emissions | |
| $D_s$ | Average Crystallite Size | nm |
| E | Electric Field | V/cm |
| **Symbol** | **Description** | **Unit** |
| $E_a$ | Activation Energy | eV |
| $E_A$ | Acceptor Energy Level | |
| EBE | Electron Beam Evaporation | |
| ED | Electro Deposition | |
| $E_D$ | Donors Energy Level | |

| EDX | Energy-Dispersive X-Ray Spectroscopy | |
|---|---|---|
| $E_{exc}$ | Electronic Excitation Energy | eV |
| $E_F$ | Fermi Level | eV |
| $E_g$ | Energy Gap | eV |
| $E_i$ | Activation Energy for Donors | eV |
| $E_U$ | Urbach Energy | eV |
| $eV_{air}$ | Schottky Barrier at Grains in Air | eV |
| $eV_{gas}$ | Schottky Barrier at Grains in Gas | eV |
| FE | Flash Evaporation | |
| FESEM | Field Emission Scanning Electron Microscopy | |
| FTS | Face Target Sputtering | |
| FWHM | Full Width at Half Maximum | Radian |
| G | Gain | |
| $G_{air}$ | Conductance of the Sensor in the Air | $(\Omega .cm)^{-1}$ |
| GDS | Glow Discharge Sputtering | |
| $G_{gas}$ | Conductance of the Sensor in the Gas | $(\Omega .cm)^{-1}$ |
| $G_o$ | Conductance at a Temperature of (273) K | $(\Omega. cm)^{-1}$ |
| Gpa | Gaga Pascal | |
| $G_s$ | Average Grain Size | nm |
| h | Plank's Constant | J.s |
| hυ | Photon Energy | eV |
| HJ | Phtodetector | |
| **Symbol** | **Description** | **Unit** |
| hkl | Millar Indices | |
| $I_a$ | Forward Current | μA |
| IBS | Ion Beam Sputtering | |
| $I_d$ , $I_{ph}$ | Dark Current , Photocurrent | μA |
| IR | Infrared | |

| | | |
|---|---|---|
| $I_s$ | Reverse Saturation Current | μA |
| I-V | Current- Voltage | |
| J | Current Density | $\mu A/cm^2$ |
| JCPDS | Joint Committee on Powder Diffraction Standards | |
| $J_S$ | Saturation Current Density in Dark | $\mu A/cm^2$ |
| k | Wavenumber | $cm^{-1}$ |
| $k_B$ | Boltzmann's Constant | J/K |
| $k_o$ | Extinction Coefficient | |
| L | Distance between the Electrode | cm |
| LA | Longitudinal Acoustic | |
| LCVD | Laser Chemical Vapor Deposition | |
| LE | Laser Evaporation | |
| LEDs | Light Emitting Diodes | |
| LO | Longitudinal | |
| LPE | Liquid Phase Epitaxy | |
| MBE | Molecular Beam Epitaxy | |
| MgO | Magnesium Oxide | |
| MOCVD | Metal Organo Chemical Vapor Deposition | |
| MOVPE | Metal Organic Vapor Phase Epitaxy | |
| MS | Magnetron Sputtering, | |
| MSM | Metal-Semiconductor-Metal | |
| n | Refractive Index | |
| **Symbol** | **Description** | **Unit** |
| N | Gas Concentration | $cm^{-3}$ |
| $N_2$ | Nitrogen | |
| NBE | Near Band Edge Emission | |
| $N_d$ | Charge-Carrier Density | $cm^{-3}$ |
| $n_e$ | Electron Concentration | $cm^{-3}$ |

| NEP | Noise Equivalent Power | |
|---|---|---|
| $N_\ell$ | Number of Layers | |
| NP | Nanoparticles | |
| NRs | Nanorods | |
| $N_s$ | Number of the Surface States | $cm^{-3}$ |
| NTCR | Negative Temperature Coefficient of Resistance | |
| NWs | Nanowalls | |
| $O_i$ | Interstitial Oxygen | |
| OCP | Open Circuit Potential | |
| OM | Optical Microscopy | |
| p | Hole Concentration | $cm^{-3}$ |
| PC | Photoconductive | |
| PCVD | Photo Chemical Vapor Deposition | |
| PD | Photodetector | |
| PECVD | Plasma Enhanced Chemical Vapor Deposition | |
| PG | Photocurrent Gain | |
| $P_{gas}$ | Partial Pressure of the Reducing Gas in the Air | mbar |
| $P_{in}$ | Incident Optical Power | mW |
| PL | Photoluminescence | |
| PLD | Pulsed Laser Deposition | |
| PM | Physical Methods | |
| PTCR | Positive Temperature Coefficient of Resistance | |
| **Symbol** | **Description** | **Unit** |
| PV | Photovoltaic | |
| q=e | Electron Charge | Coulomb |
| QE | Quantum Efficiency | |
| R | Film Resistance | Ω |
| $R_a$ | Electric Resistance of the Sensor in Air | Ω |

| | | |
|---|---|---|
| $R_e$ | Reflectance | |
| RF | Radio Frequency | |
| $R_F$ | Rectification Ratio | |
| $R_g$ | Electric Resistance of the Sensor in Presence of Gas | Ω |
| RH | Resistive Heating | |
| $R_H$ | Hall Coefficient | $cm^3/C$ |
| RMS | Root Mean Square | nm |
| RSS | Raman Scattering Spectroscopy | |
| RT | Room Temperature | |
| $R_\lambda$ | Responsivity | mA/W |
| S | Microstrains | $lin^{-2}m^{-4}$ |
| SCM | Spin Coating Method | |
| SEM | Scanning Electron Microscopy | |
| SGS | Semiconductor Gas Sensor | |
| SGT | Solution Growth Technique | |
| Si | Silicon | |
| SILAR | Ideality Factor, Successive Ion Layer Adsorption and Reaction | |
| $SO_2$ | Sulphur Dioxide | |
| $S_t$ | Sensitivity of Sensors | |
| t | Film Thickness | nm |
| T | Temperature | K |
| TA | Transverse Acoustic | |
| **Symbol** | **Description** | **Unit** |
| TCOs | Transparent Conductive Oxides | |
| TFTs | Thin Film Transistors | |
| TO | Transverse | |
| $T_r$ | Transmittance | |
| $t_r$ | Transit Time | s |

| | | |
|---|---|---|
| TS | Triode Sputtering | |
| UV | Ultraviolet | |
| UV-Vis | Ultraviolet-Visible | |
| v | Velocity of Propagation | m/s |
| V.B | Valence Band | |
| $V_a$ | Forward Bias Voltage | V |
| $V_{bi}$ | Built-in- Potential | eV |
| VE | Vacuum Evaporation | |
| $V_H$ | Hall Voltage | V |
| $V_o$ | Oxygen Vacancy | |
| $V_{Zn}$ | Zinc Vacancy | |
| **w** | Depletion Width Layer | nm |
| X-RD | X-Ray Diffraction | |
| y | Characteristic Exponent, Lower than (1) | |
| $Zn_i$ | Interstitial Zinc | |
| ZnO | Zinc Oxide | |
| $B'$ | Inversely Proportional to Amorphusity | |
| $n_c$ | Refractive Index of Complex | |
| $\tau$ | Carrier’s Lifetime | s |
| $\mu_p$ | Mobility of Electron | $cm^2/V.s$ |
| $\mu_n$ | Mobility of Hole | $cm^2/V.s$ |
| $V_d$ | Drift Velocity | m/s |

| Symbol | Description | Unit |
|---|---|---|
| $\sigma_o$ | Minimum Electrical Conductivity at (0)K | $(\Omega. cm)^{-1}$ |
| $\rho$ | Resistivity | $(\Omega. cm)$ |
| $\Delta$ | Lattice Mismatch | |
| $\lambda_c$ | Cutoff Wavelength | nm |
| $\ell$ | Distance Between Electrodes | cm |

| $\Phi_s$ | Surface Barrier Height | nm |
|---|---|---|
| $\lambda$ | Wavelength | nm |
| $\beta$ | Full Width at Half Maximum | radian |
| $\gamma$ | Tunneling Factor | |
| $\eta$ | Ideality Factor | |
| $\theta_B$ | The Bragg's Angle | degree |
| $\lambda_o$ | Free Space Wavelength | nm |
| $\delta_D$ | Dislocation Density | line $m^{-2}$ |
| $\sigma_{D.C}$ | Electrical Conductivity | $(\Omega.cm)^{-1}$ |
| $\alpha$ | Absorption Coefficient | $cm^{-1}$ |
| $\Delta f$ | Bandwidth | Hz |
| $\varepsilon_i$ | Imaginary of Dielectric Constant | F/cm |
| $\varepsilon_r$ | Real Imaginary of Dielectric Constant | F/cm |
| $\varepsilon_s$ | Semiconductor Permittivity's | F/cm |
| $\theta'$ | Fractional Occupancy | |
| $\lambda_m$ | Maximum Wavelength | nm |
| $\upsilon$ | Frequency | Hz |
| $\Phi_B$ | Barrier Height | nm |
| $\Phi_m$ | Work Function | eV |
| $\chi$ | Electron Affinities | |
| $'n$ | Electron | |

## List of Figures


| Figure No. | Description | Page No. |
|---|---|---|
| 1.1 | The Hexagonal Wurtzite Structure of ZnO. | 2 |
| 1.2 | Stick and Ball Representation of ZnO Crystal Structures: (a) Cubic Rock Salt, (b) Cubic Zinc Blend, and (c) Hexagonal Wurtzite. | 5 |
| 1.3 | Schematic Diagram of NaCl-Type Crystal Structure for MgO | 6 |

| | | |
|---|---|---|
| 1.4 | The Diamond Lattice Structure for Si. | 10 |
| 1.5 | Classification of Thin Film Depositions Technique. | 11 |
| 1٢, | Schematic of the Stokes and anti-Stokes Transition with a Raman Shift. | 25 |
| 2٢, | Schematic Diagram Showing the Types of Transition of the Electrons ,Rayleigh and Raman Scattering. | 26 |
| 2.3 | Energy-Band for two Isolated Semiconductors of Opposite Types and Different $E_g$ (a) the Smaller Band Gap is n-Type and (b) the Bigger Band Gap is p-Type. | 35 |
| 2.4 | Fig. 2.4: Classification of Phtodetectors as (a) straddling, (b) staggered, and (c) broken-gap. | 36 |
| 5٢, | Photoconductive Detector. | 42 |
| 6٢, | Processes of Photoconductive for Semiconductor (a) Intrinsic , and (b) Extrinsic. | 43 |
| 7٢, | Application of a Common Semiconductor Sensor is to Monitor a Physical Quantity through the Change of Electrical Signal. | 46 |
| 8٢, | The Oxygen Vacancies at the Surface of the Grain. | 49 |
| 9٢, | The Potential Barrier at the Interface of n-Type Metal Oxide. | 50 |
| 3.1 | Schematic Diagram of the Experimental Work. | 54 |
| 3.2 | Schematic of Spray Pyrolysis Equipment. | 55 |
| 3.3 | The Masks used for (a) D.C Measurement, and (b) Hall Effect. | 58 |
| 3.4 | The Operation Principle of AFM. | 60 |
| 3.5 | Image of Gas Sensor Testing System | 64 |
| 3.6 | Schematic Diagram of Interdigital Electrodes | 65 |
| **Figure No.** | **Description** | **Page No.** |
| 3.7 | Photographic Plate of Photoconductive Mask, and Samples of ZnO /n-Si Gas Sensor and $Mg_xZnO_{1-x}$ / n-Si Gas Sensor | 65 |
| 3.8 | Schematic Diagram of Gas Sensing and the Electrical Circuit Setup for Gas Sensing Measurements. | 66 |
| 4.1 | XRD Patterns for ZnO Thin Films. | 68 |

| | | |
|---|---|---|
| 4.2 | XRD Patterns for $Mg_xZnO_{1-x}$ Thin Films With Different Mg-Content ,at Substrate Temperature (400) °C. | 73 |
| 4.3 | XRD Patterns for $Mg_xZnO_{1-x}$ Thin Films With Different Mg-Content, at Substrate Temperature (450) °C. | 74 |
| 4.4 | XRD Patterns for Thin $Mg_xZnO_{1-x}$ Thin Films With Different Mg-Content, at Substrate Temperature (500) °C. | 76 |
| 4.5 | Variation of (a and c axis) Lattice Constants vs. Different Mg-Content for $Mg_xZnO_{1-x}$ Thin Films. | 79 |
| 4.6 | Variation of FWHM, $D_S$ ,S, and $\delta_D$ vs. Different Mg-Content for $Mg_xZnO_{1-x}$ Thin Films , at Different Substrate Temperatures. | 79 |
| 4.7 | 3-D AFM Image and Granularity Accumulation for $Mg_xZnO_{1-x}$ with Different Mg- Content, at Substrate Temperature (400) °C. | 85 |
| 4.8 | 3-D AFM Image and Granularity Accumulation for $Mg_xZnO_{1-x}$ with Different Mg-Content, at Substrate Temperature (450) °C. | 86 |
| 4.9 | 3-D AFM Image and Granularity Accumulation for $Mg_xZnO_{1-x}$ with Different Mg-Content , at Substrate Temperature (500) °C. | 87 |
| 4.10 | Transmittance as a Function of Wavelength for $Mg_xZnO_{1-x}$ , at Substrate Temperatures (400 ,450, and 500) °C. | 90 |
| 4.11 | Absorbance as a Function of Wavelength for $Mg_xZnO_{1-x}$ (a=400 , b=450 , and c=500) °C. | 92 |
| 4.12 | Reflectance as a Function of Wavelength for $Mg_xZnO_{1-x}$ at Substrate Temperatures (400,450,and 500) °C. | 93 |
| 4.13 | Absorption Coefficient as a Function of Wavelength for $Mg_xZnO_{1-x}$ , at $T_s$ (a=400,b=450, and c=500) °C. | 95 |
| 4.14 | $(\alpha h\upsilon)^2$ Versus Photon Energy for $Mg_xZnO_{1-x}$ , at $T_s$ (400) °C. | 96 |
| 4.15 | $(\alpha h\upsilon)^2$ Versus Photon Energy for $Mg_xZnO_{1-x}$ , at $T_s$ (450) °C. | 97 |
| **Table No.** | **Description** | **Page No.** |
| 4.16 | $(\alpha h\upsilon)^2$ Versus Photon Energy for $Mg_xZnO_{1-x}$ , at $T_s$ (500) °C. | 98 |
| 4.17 | Refractive Index as a Function of Wavelength for $Mg_xZnO_{1-x}$ , at $T_s$ (a=400,b=450 , and c=500) °C. | 99 |
| 4.18 | The Extinction Coefficient as a Function of Wavelength for $Mg_xZnO_{1-x}$ , at $T_s$ (a=400, b=450 , and c=500) °C. | 100 |

| Figure No. | Description | Page No. |
|---|---|---|
| 4.19 | Variation of $\varepsilon_r$ and $\varepsilon_i$ as a Function of Wavelength for $Mg_xZnO_{1-x}$(a1,a2=400, b1,b2=450, and c1,c2=500) °C. | 102 |
| 4.20 | PL Spectra of Pure ZnO Thin Films at Substrate Temperatures (400, 450, and 500)°C. | 104 |
| 4.21 | PL Spectra of $Mg_xZnO_{1-x}$ Thin Films Grown on Glass Substrate Temperatures (a=400, b=450 , and c=500)°C. | 105 |
| 4.22 | $\ln\sigma_{D.C}$ Versus 1000/T for $Mg_xZnO_{1-x}$ Thin Films at Different Mg-Content, at $T_s$ (450) °C. | 108 |
| 4.23 | $\ln\sigma_{D.C}$ Versus 1000/T for $Mg_xZnO_{1-x}$ Thin Films at Different Mg-Content, at $T_s$ (500) °C. | 109 |
| 4.24 | The $\rho$ , $\sigma_{D.C}$ , $\mu_H$ ,and n Versus Mg-Content for $Mg_xZnO_{1-x}$ Thin Films, at $T_s$ (400,450,and 500) °C. | 111 |
| 4.25 | FESEM and EDS for $Mg_xZnO_{1-x}$ /n-Si Photodetector for Mg-Content (0,30,and 50) at (450) °C. | 113 |
| 4.26 | FESEM and EDS for $Mg_{x.}ZnO_{1-x}$/n-Si Photodetector for Mg-Content (70, and 90) at 450) °C. | 114 |
| 4.27 | FESEM and EDS for $Mg_{0.3}ZnO_{0.7}$ /n-Si Phtodetector at Substrate Temperatures (400,450,and 500) °C. | 116 |
| 4.28 | PL Spectra of $Mg_{0.3}ZnO_{0.7}$ / n-Si Photodetector with Different $T_s$ (400, 450, and 500)°C. | 119 |
| 4.29 | PL Spectra of $Mg_xZn_{1-x}O$ /n-Si Photodetector with Different Mg-Content at $T_s$(450)°C. | 119 |
| 4.30 | Raman Shift for $Mg_xZnO_{1-x}$/n-Si Photodetector Prepared in Different Mg-Content , at Substrate Temperature (450) °C. | 122 |
| 4.31 | Raman Shift for $Mg_{0.3}ZnO_{0.7}$/n-Si Photodetector Prepared, at Different Substrate Temperatures. | 123 |
| 4.32 | The Variation of Capacitance as a Function of Voltage for Al/Mg ZnO/ n-Si/Al Photodetector (PDs) with Different Mg-Contents (0,30,50, 70, and 90), and $T_s$ (450) °C. | 125 |
| 4.33 | The Variation of Capacitance as a Function of Voltage for Al/$Mg_{0.3}ZnO_{0.7}$/ n-Si/Al Photodetector (PDs) with Different Substrate Temperatures. | 126 |
| **Figure No.** | **Description** | **Page No.** |
| 4.34 | The Variation of ($1/C^2$) as a Function of Reverse Bias Voltage at Different Mg-Content (0 ,30, 50,70,and 90) for $Mg_xZnO_{1-x}$ /n-Si Photodetector at Substrate Temperature (450)°C | 127 |
| 4.35 | The Variation of ($1/C^2$) as a Function of Reverse Bias Voltage for $Mg_{0.3}ZnO_{0.7}$ /n-Si Photodetector at Different | 128 |

| | | |
|---|---|---|
| | Substrate Temperature. | |
| 4.36 | I-V Characteristics in the Dark for $Mg_xZnO_{1-x}$ /n-Si Photodetector (a- Forward ,b- Reverse, c- Forward (30)% at $T_s$ (450, and 500)$^oC$. | 130 |
| 4.37 | I-V Characteristics at Forward Bias Voltage on a Semilogarithim Scale for $Mg_xZnO_{1-x}$/n-Si Photodetector, at Different Mg-Content (x). | 131 |
| 4.38 | I-V Characteristics at Forward Bias Voltage on a Semilogarithim Scale for $Mg_{0.3}ZnO_{0.7}$ /n-Si Photodetector, at Different Substrate Temperatures . | 131 |
| 4.39 | The I-V Characteristics at Different Incident Power Intensity for $Mg_xZnO_{1-x}$/n-Si Photodetector at Reverse Bias Voltage. | 133 |
| 4.40 | The Photocurrent and Dark Current as a Function of Forward Bias Voltage for $Mg_xZnO_{1-x}$ /n-Si Photodetector , at Different Mg-Content (0,30,50,760,and 90). | 135 |
| 4.41 | The Photocurrent and Dark Current as a Function of Forward Bias Voltage for $Mg_{0.3}ZnO_{0.7}$ /n-Si Photodetector , at Different Substrate Temperatures. | 136 |
| 4.42 | The Variation of Responsivity as a Function of Wave length for $Mg_xZnO_{1-x}$/n-Si Photodetector (a- at Different Mg-Content , b- at Different Substrate Temperatures). | 137 |
| 4.43 | The Variation of Quantum Efficiency as a Function of Wavelength for $Mg_xZnO_{1-x}$ /n-Si Photodetector (a- at Different Mg-Contents ,b- at Different $T_s$). | 138 |
| 4.44 | The Variation of Specific Detectivity as a Function of Wavelength for $Mg_xZnO_{1-x}$ /n-Si Photodetector (a- at Different Mg-Content , b- at Different Temperatures). | 139 |
| 4.45 | The Variation of (NEP) as a Function of Wavelength for $Mg_xZnO_{1-x}$ /n-Si Photodetector (a- at Different Mg-Content, and b- at Different $T_s$). | 140 |
| **Figure No.** | **Description** | **Page No.** |
| 4.46 | The Variation of Sensitivity with the Different Operating Temperature of the Prepared $Mg_{0.05}ZnO_{0.95}$/n-Si Gas Sensor{a- at Temperatures (450,and 500) $^oC$, and b- at both Substrate Temperatures (400, and 450) $^oC$ }. | 142 |
| 4.47 | The Variation of Response and Recover Time with | 144 |

| | Different Operating Temperatures for $Mg_xZnO_{1-x}$/n-Si Sensor at Substrate Temperatures (400,450, and 500) $^oC$. | |
|---|---|---|


## List of Tables


| Table No. | Description | Page No. |
|---|---|---|
| 1.1 | Semiconductor Properties of ZnO. | 4 |
| 1.2 | Semiconductor Properties of MgO. | 8 |
| 1.3 | Properties of Crystal Si Semiconductors at 300K. | 10 |
| 3.1 | Chemical Materials that used in the Preparation. | 53 |
| 4.1 | Structural Properties of ZnO Thin Films prepared on Glass Substrate Temperatures (400,450, and 500) $^oC$. | 69 |
| 4.2 | The $D_s$ , $\delta_D$, S, and $N_l$ of Layers Data of (002),(200) Orientations for $Mg_xZnO_{1-x}$ at Different Mg-Content, at Substrate Temperature (400) $^oC$. | 72 |
| 4.3 | The $D_s$ , $\delta_D$, S, and $N_l$ of Layers Data of (002),(200) Orientations for $Mg_xZnO_{1-x}$ at Different Mg-Content, and Substrate Temperature (450) $^oC$. | 75 |
| 4.4 | The $D_s$ , $\delta_D$, S, and $N_l$ of Layers Data of (002),(200) Orientations for $Mg_xZnO_{1-x}$ at Different Mg-Content, and Substrate Temperature (400) $^oC$. | 77 |
| 4.5 | Average Diameter,Total Grain No., Surface Thickness, Roughness Average and Root Mean Square for $Mg_xZnO_{1-x}$ Thin Films at Different Mg- Contents (0,30,50,70, and 90), and Different Temperatures (400, 450,and 500) $^oC$. | 84 |
| 4.6 | Activation Energies for $Mg_xZnO_{1-x}$ Thin Films at Different Mg-Content of (x), and Substrate Temperature (450) $^oC$. | 107 |
| Table No. | Description | Page No. |
| 4.7 | Comparison between the Crys. Size calculated from (XRD) and (FESEM) Analysis for $Mg_xZnO_{1-x}$/n-Si Photodetector. | 115 |
| 4.8 | Comparison between the Crys. Size calculated from (XRD) and (FESEM) Analysis for $Mg_{0.3}ZnO_{0.7}$ /n-Si | 115 |

| | | |
|---|---|---|
| | Photodetector at Different Substrate Temperatures. | |
| 4.9 | Compound Percentage of the $Mg_xZnO_{1-x}$ /n-Si Photodetector. | 115 |
| 4.10 | Wavelength and Energy Values of Photoluminescence Peaks for $Mg_xZnO_{1-x}$/n-Si Photodetector at Different Substrate Temperatures , and (30)% Mg-Content. | 120 |
| 4.11 | Wavelength and Energy Values of Photoluminescence Peaks for $Mg_xZnO_{1-x}$/n-Si Photodetector at Different Mg-Content , and Substrate Temperature (450)$^o$C. | 120 |
| 4.12 | The Variation of the $C_o$, W, $V_{bi}$ , and $N_D$ for $Mg_xZnO_{1-x}$/n-Si Photodetector at Different Mg-Content of (x). | 126 |
| 4.13 | The Variation of the $C_o$ ,W ,$V_{bi}$ , and $N_D$ for $Mg_xZnO_{1-x}$ Photodetector at Different Substrate Temperatures. | 128 |
| 4.14 | Values of Ideality Factor (η), Saturation Current ($I_s$) for $Mg_xZnO_{1-x}$ /n-Si Photodetector at Different Mg-Content of (x). | 132 |
| 4.15 | Values of Ideality Factor (η), and Saturation Current ($I_s$) for $Mg_{0.3}ZnO_{0.7}$ /n-Si Photodetector at Different Substrate Temperatures. | 132 |
| 4.16 | The Variation of the Photocurrent , Dark Current and the Gain for $Mg_xZnO_{1-x}$/n-Si Photodetector at Different Mg-Content, at $T_s$ (450) $^o$C. | 134 |
| 4.17 | The Variation of the Photocurrent , Dark Current and the Gain for $Mg_{0.3}$ $ZnO_{0.7}$ /n-Si Photodetector, at Both Substrate Temperatures (450 , and 500) $^o$C. | 135 |
| 4.18 | The Response Time and the Recovery Time with Different Operating Temperatures of $Mg_xZnO_{1-x}$ /n-Si Photodetector with Different Mg-Content, at Substrate Temperature (400) $^o$C. | 143 |


## 1.1 Introduction

Semiconductors are a group of materials having electrical conductivity between metals and insulators. The semiconductors materials have electrical properties as a

function of temperature, optical excitation, magnetic field, electromagnetic, and impurity content multicomponent materials like compound semiconductor and their alloys are of considerable technical interest in the field of electronic and optoelectronic devices [1].

It is difficult to prepare these materials in bulk form due to the limited solubility of materials in each other, in addition their growth is costly process [2]. From this point much effort has been taken to prepare thin films. In thin films, deviation from the properties of the corresponding bulk materials arise because of their small thickness, large surface to volume ratio and unique physical structure which is a direct consequence of the growth process [3].

The physics of semiconductor nanostructures has attracted great interest for many years because these are systems of reduced dimensionality with properties different from bulk semiconductor properties. These systems lead to confinement of carriers and elementary excitations in one or more directions, exhibit new quantum phenomena and offer great deal of flexibility of tailoring the electronic and optical properties for specific purposes photodetectors (PD) are optical sensor devices which are able to convert light into electrical signals using the principles of photoconductivity[4].

When light with sufficient energy is absorbed by certain semiconductors, the number of free carriers increases which leads to enhanced photoconductivity compared to dark conditions [5]. $Mg_xZn_{1-x}O$ belong to the class of transparent conductive oxides (TCOs).TCOs are a unique class of materials, because they exhibit both, transparency and electronic conductivity, simultaneously[6].

Usually, conductive materials, such as metals, are not transparent, while transparent materials, such as insulators, are not conductive. TCOs combine these two properties due to their large energy gap ($\geq$ 3 eV), leading to the transparency in the visible spectrum of the light, and a low effective mass of the electrons, which can be attributed to the high dispersion and the s-type character of the conduction band, explaining the high conductivity[7,8].

The gas sensing characteristics of the materials can be improved by incorporating some additives into oxide films. Catalysts like (In, Pt, Pd, Ag, Au, and Cu) often added to the based material to improve the gas sensitivity and selectivity [9]. The adsorption and desorption gas sensing mechanism of semiconductor gas sensor is the simple resistivity change.

The surface morphology is controlled by varying the deposition parameters. The control of the surface morphology is of particular interest for gas sensor applications where a porous morphology is desired to increase the adsorption and implicitly the sensor response to specified gas [10].

## 1.2 Crystal Structure of ZnO

Zinc oxide (ZnO) crystallize preferentially in the stable hexagonal wurtzite structure at room temperature and normal atmospheric pressure as shown in fig.1.1. It has lattice parameters a= (3.250) Å, c = (5.206) Å with a density of (5.606) g. $cm^{-3}$.

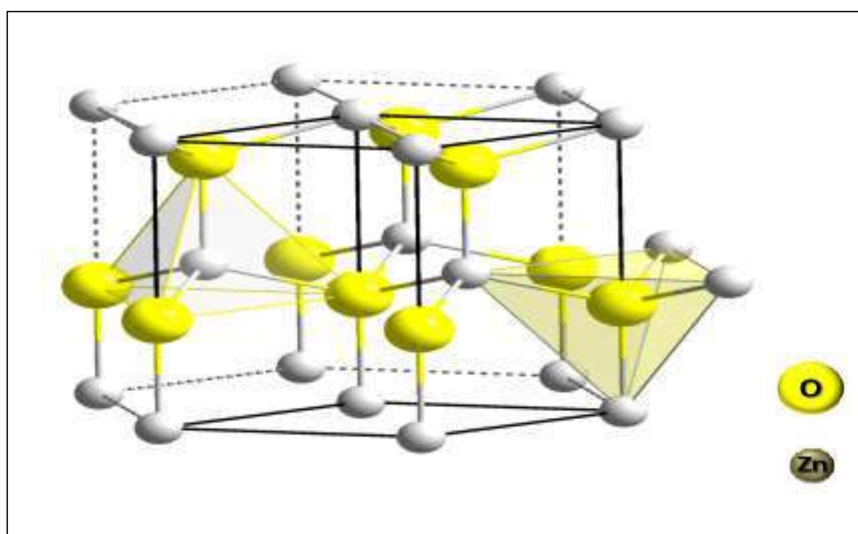


Fig.1.1: The Hexagonal Wurtzite Structure of ZnO. One Unit Cell of the Crystal is out Lined for Clarity [11].

The electronegativity values of $O^{-2}$ and $Zn^{+2}$ are (3.44) and (1.65), respectively resulting in very strong ionic bonding between $Zn^{+2}$ and $O^{-2}$. Its wurtzite structure is very simple to explain, where each oxygen ion is surrounded tetrahedral by four Zinc ions, and vice versa, stacked alternatively along the c-axis. It is clear that this kind of tetrahedral arrangement of $O^{-2}$ and $Zn^{+2}$ in ZnO will form a non central symmetric structure composed of two interpenetrating hexagonally closed packed sub-lattices of

Zinc and oxygen that are displaced with respect to each other by an amount of (0.375) along the hexagonal axis.

This is responsible for the piezoelectricity observed in ZnO, and it also plays a vital role in crystal growth, defect generation and etching [8]. Other basic characteristics of ZnO are the polar surfaces that are formed by oppositely charged ions produced by positively charged $Zn^{+}$(0001) and negatively charged $O^{-}$ ($000\bar{1}$) polar surfaces. It is responsible for the spontaneous polarization observed in ZnO.

The polar surfaces of ZnO have non-transferable and non-flowable ionic charges [12]. The semiconductor properties of ZnO are shown in table 1.1.

Table 1.1: Semiconductor Properties of ZnO [13]

| Properties | Value |
|---|---|
| Molecular Weight | (81.38) g. $mol^{-1}$ |
| Melting Point | (1975) $^{o}C$ |
| Boiling Point | (2360) $^{o}C$ |
| Density | (5.606) g. $cm^{-3}$ |
| Appearance | White Solid |
| Crystal Structure | Hexagonal Wurtzite |

| Direct Energy Gap at (300) K | (3.4) eV |
|---|---|
| Odor | Odorless |
| Solubility in Water | Insoluble |
| Lattice Constant | a = (3.250) Å , c = (5.206) Å |
| Electronegativity | 1.65 |
| Refractive Index | (2.0041) |
| Wavelength | (365) nm |
| Exciton Binding Energy | (60) meV |
| Dielectric Constant | (9.0) |
| Electron Effective Mass | (0.24) |
| Hall Effective Mass | (0.59) |
| Type of Conductivity | n-type |

### 1.2.1 Basic Crystal Structures of ZnO

ZnO crystallizes in three forms: hexagonal wurtzite, cubic Zinc blende, and cubic rock salt. The wurtzite structure is most stable at ambient conditions and thus most common. The Zinc blende form can be stabilized by growing ZnO on substrates with cubic lattice structure. In both cases, the Zinc and oxide centers are tetrahedral.

The rock salt (NaCl-type) structure is rarely observed and it is only observed at relatively high pressures of about (10) Gpa. These basic structures are shown in fig.1.2. Despite of these three basic forms ZnO can be induced to form a very large variety of crystalline shapes using specialized growth methods [14].

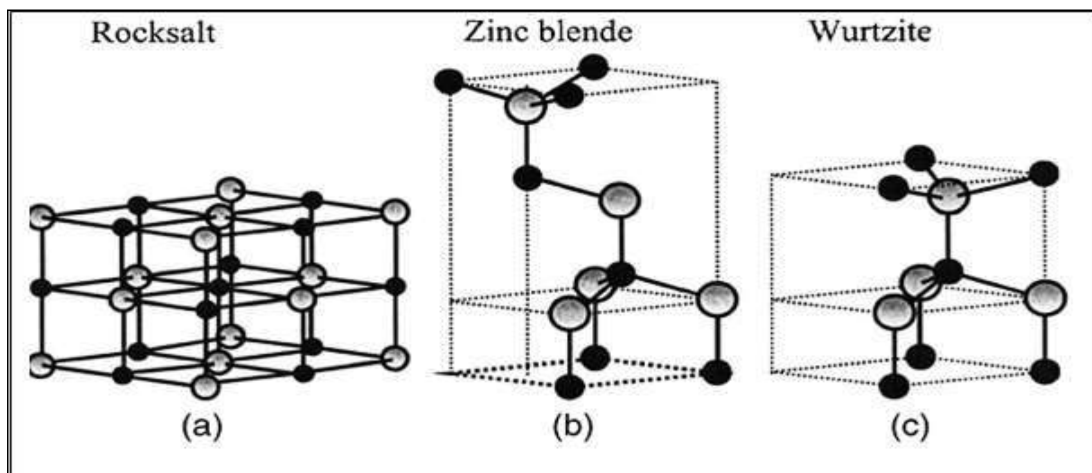


Fig.1.2: Stick and Ball Representation of ZnO Crystal Structures:
(a) Cubic Rock Salt, (b) Cubic Zinc Blende, and (c) Hexagonal Wurtzite [14].

### 1.2.2 Applications of ZnO

ZnO is attracting much attention for its application to UV light-emitters, varistors, transparent high power electronics, surface acoustic wave devices, piezoelectric transducers and as a window material for display and solar cells a common application is in gas sensors. Recent improvements in the quality and control of conductivity in bulk and epitaxial ZnO have increased interest in the use of this material for short wavelength light emitters and transparent electronics [15]. It has been utilized in recent research to build blue light emitting diodes (LEDX) and transparent thin film transistors (TFTs). ZnO is a candidate for solid state blue to UV optoelectronics, including lasers[16]. Compared to those deposited on glass substrates making the devices portable. They can be used in plastic liquid crystal displays, transparent electromagnetic shielding materials, flexible electro-optical devices, touch sensitive overlay and unbreakable heat-reflecting mirrors [17]. It has wide applications in electronic devices, such as transparent conductors, varistors (variable resistors), ultra violet laser sources and ultraviolet detectors. Regarding the materials processing point of view, both doped-and undoped bulk-ZnO are relatively easy to process and result in a stochiometrical very stable compound. In medical applications, ZnO works to prevent sunburn but is also used to treat nappy rash, skin irritations, cold sores, cuts and burns[18].

## 1.3 Magnesium Oxide Thin Films, and its Applications

Magnesium oxide (MgO) is a highly ionic crystalline solid which crystallized into a rock salt structure, it has (FCC) $Mg^{+}$ and $O^{-}$ sublattice and low energy neutral (100) cleavage planes, viewed as an arrangement of hard sphere bound together by electrostatic forces. In an MgO unit cell (14) oxygen ions are closed packed into a face-centered cubic structure, while (12) magnesium ions are located at the center of the cube edges and one magnesium ion located at the cube center shown in fig.1.3 [19].

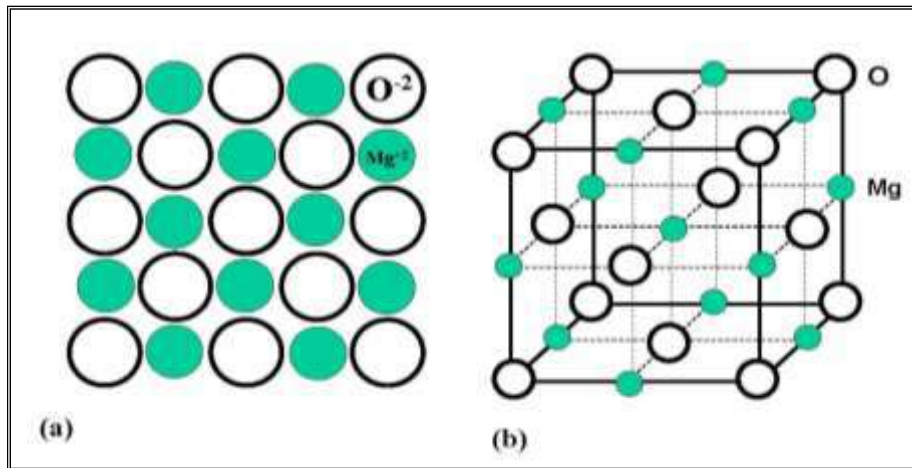


Fig.1.3: Schematic Diagram of NaCl-type Crystal Structure for MgO,
(a) 2-D, and (b) 3-D [19].

Researchers have been focused much attention on the one applications in nanoelectronic devices. MgO is a typical wide energy gap (7.8) eV insulator, represents an important class of functional metal oxides with a broad range of properties. Also they find tremendous application in catalysis, refractory industries, electronics, cosmetics and waste water remediation [20].

MgO performs excellently in high temperature, particularly in the creation of electrical insulation. Other properties of MgO include effective corrosion resistance and that it is transparent to (IR) light. It has a high thermal and low electrical conductivity [21]. The vast applications of MgO nanomaterial inclined to work on this material. Here for various morphologies of MgO such as nanorods, nanobelts nanowires, nanosheets, and nanoplate [22] have been synthesized via a variety of different chemical routes annealed temperature on the particle size, morphology and luminescent properties of the MgO nanomaterial were MgO, or magnesia, is a white solid metal that occurs naturally as periclase. It has an empirical formula of MgO.

The antibacterial activities of MgO nanoparticles (MgONP) alone or in combination with other antimicrobials (nisin and ZnO NP) against Escherichia coli $O_{157}$:$H_7$ and Salmonella Stanley were investigated. The results show that (MgO NP) have strong bactericidal activity against the pathogens, achieving more than 7log reductions in bacterial counts [23]. The general properties of magnesium oxide are

shown in table1.2. Initially MgO is used as the principal ingredient in the construction materials used for moisture resistance and fire proofing. In steel furnace linings, it is used as a refractory. Other applications include polycrystalline ceramic for aircraft wind shields, electrical insulation, pharmaceuticals and cosmetics, inorganic rubber accelerator, oxychloride and oxysulfate cements, paper manufacture, fertilizers, removal of sulphur dioxide ($SO_2$) from stack gases, adsorption and catalysis, food and feed additive. MgO is one of the thermodynamically high stable materials. It has a low refractive index and dielectric constant (~ 9.8). Due to these excellent properties, MgO has been widely used in the applications for high frequency devices and high speed switching devices [24]. It is used as substrate for growing thin film materials.

Table 1.2: Semiconductor Properties of MgO[25].

| Properties | Value |
|---|---|
| Molecular Weight | (40.31) g. mol $^{-1}$ |
| Melting Point | (٢٨٥٢) °C |
| Boiling Point | (٣٦٠٠) °C |
| Density | (٣,٥٨) g. cm $^{-3}$ |
| Appearance | White to grey powder |
| Crystal Structure | Cubic (FCC) |
| Energy Gap | (7.8) eV |
| Odor | Odorless |
| Solubility in Water | Soluble in acid and ammonia insoluble in alcohol. |
| Lattice Constant | a = (4.212)Å |

| Electronegativity | 1.31 |
| --- | --- |
| Refractive Index | 1.73 |
| Wavelength | (159) nm |
| Exciton Binding Energy | (80) meV |
| Dielectric Constant | (9.83) |
| Type of Conductivity | p-type |

### 1.4 The p-$Mg_xZnO_{1-x}$ Tin Film

ZnO and MgZnO are group II-VI wide-energy gap materials that are currently under intense study as blue and ultraviolet light-emitting diodes (LEDX). In particular, its large exciton binding energy of (60) meV, which is larger than the thermal energy at room temperature (RT), allows excitons to play important roles at (RT) and ensures efficient lasing even at (RT). In general, Mg is incorporated as substitution type materials to control the energy gap in ternary oxide semiconductors. Although $Mg^{+2}$ (0.57) Å has a similar ionic radius to $Zn^{+2}$ (0.60) Å, the solid solubility of MgO in the ZnO matrix is limited due to its different crystal structure.

MgO has a cubic rock salt structure, while ZnO has a hexagonal wurtzite structure. So, the reports have demonstrated that the MgZnO alloy with a wide range of $Mg^{+2}$ from (0 to 36)% still maintained the hexagonal lattice structure due to the similar ionic radius of $Mg^{+2}$ and $Zn^{+2}$, and corresponding energy gap could be increased from (3.34 to 3.96) eV. Moreover, the MgZnO composite could produce a bright ultraviolet luminescence at (RT) due to the band edge exciton recombination.

The MgZnO thin films acts as an excellent candidate for ultraviolet optoelectronic devices such as UV LED, UV laser, and UV detector. Non equilibrium growth conditions vary with the preparing technique, such as pulsed laser deposition (PLD) [26-28] sputtering, metal organic vapor phase epitaxy (MOVPE) and molecular beam epitaxy (MBE), leading to a different Mg saturation concentration. Accordingly, it is worth applying various preparation methods to explore the Mg saturation content and thermal stability of the MgZnO alloys in order to better understand this material [29].

### 1.5 Crystallite Silicon

Crystallite silicon (c-Si) is an important material of the last century that has been the cornerstone of the semiconductor industry and has spearheaded extraordinary technological advancement. Bulk (c-Si), however, has an indirect band gap, making it unsuitable for integrating light with electronics (optoelectronics). Thus, (c-Si) has only very poor luminescence in the near (IR) (1100) nm region. (c-Si) is one of the most widely studied semiconductors and its properties are well known. It crystallizes in diamond structure with (FCC) braveries and lattice constant of (5.430) Å as shown in fig.1.4 [30]. Each atom of silicon has four valence electrons which occupy the tetrahedral hybridized $Sp^3$ orbital pointing towards the four nearest neighbors. The bond between two nearest neighbors is formed by two electrons with opposite spins. The general properties of (c-Si) as shown in table 1.3.

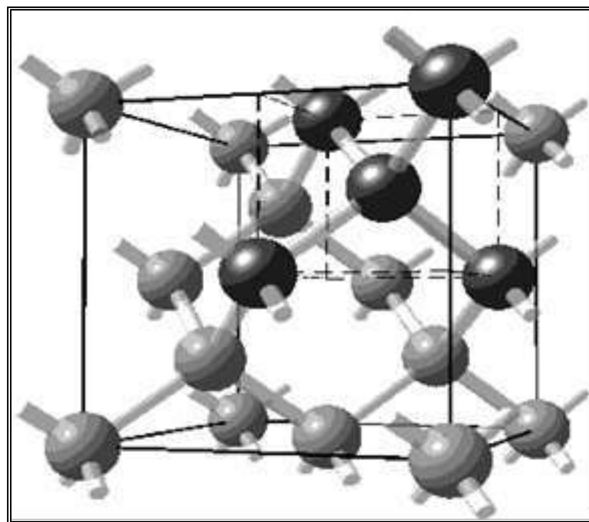

Fig.1.4:The Diamond Lattice Structure for Si [31].

Table 1.3:Properties of Crystal Si Semiconductors at 300K [32]

| Properties | Si |
|---|---|
| Molecular Weight | (28.1) g. $mol^{-1}$ |
| Melting Point | (1414) $^oC$ |
| Density | (2.329) g. $cm^{-3}$ |
| Crystal Structure | Diamond |
| Energy Gap | (1.12) eV |
| Electron Affinity | (4.05) eV |
| Dielectric Constant (ε) | 11.9 |

| Lattice Constant | (5.430)Å |
| --- | --- |
| Coefficient of Linear Expansion per Degree | $2.44 \times 10^{-6}$ |
| Mobility of Electron | (1500) $cm^2/V.s$ |
| Mobility of Hole | (450) $cm^2/V.\ s$ |
| Intrinsic Carrier Concentration | $(9.65 \times 10^9)\ cm^{-3}$ |
| Electron Affinity | (4.07) eV |
| Thermal Conductivity | (1.56) W/cm. K |
| Effective Density of State in Valence Band, ($N_v$ ) | $(2.65 \times 10^{19})\ cm^{-3}$ |
| Effective Density of State in Conduction Band, ($N_c$ ) | $(2.8 \times 10^{19})\ cm^{-3}$ |
| Minority Carrier Lifetime | $(2.5 \times 10^{-3})$ s |
| Specific Heat | (0.713) J/g.°C |
| Thermal Diffusivity | (0.9) $cm^2/\ s$ |

### 1.6 Methods of Preparing Thin Films

The methods of preparing thin film can be divided essentially into two main groups: namely physical and chemical methods. The most important physical methods for preparation of thin films are the vacuum evaporation (VE) and cathode sputtering (CS). Both methods required low pressure in working space and therefore make use of vacuum techniques. Vacuum evaporation is the most widely used methods for deposition of thin films, in this methods the atoms or molecules are liberated by heating the material using a heating source (or boat) in a vacuum system at a certain pressure. The methods employed for thin film deposition can be divided into two groups based on the nature of deposition process, namely physical and chemical as shown in fig.1.5.

Thin films deposition technique

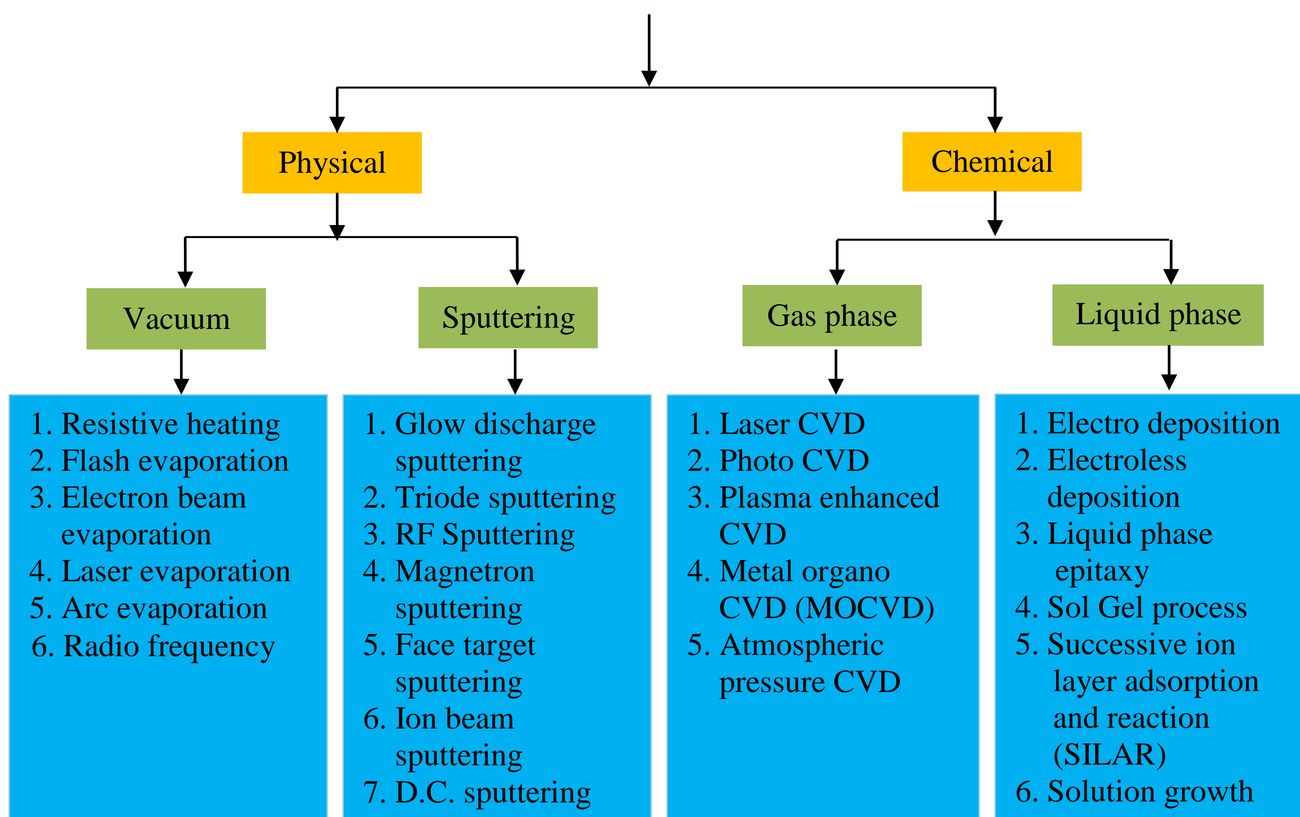


Fig.1.5: Classification of Thin Film Depositions Technique.

Chemical deposition techniques are the most important methods for growth of the films owing to their versatility for depositing large number of elements and compounds at low temperature [33].

### 1.6.1 Chemical Spray Pyrolysis Technique

This is a thermally stimulated reaction between the clusters of liquid vapour atoms of different spraying solutions of the desired compound onto a substrate maintained at elevated temperature. The sprayed droplets on reaching the hot substrate undergo pyrolytic decomposition and form a single crystal or cluster of crystallites of the product. The other volatile byproducts and excess solvents escape in the vapour phase.

The thermal energy for decomposition, subsequent recombination of the species, sintering and recrystallisation of the crystallites is proved by hot substrate. The nature of the fine spray droplets, with the help of a carrier gas depends upon spray nozzle.

The growth of a film by a spray pyrolysis is determined by nature of the substrate, solution as well as spray parameters. The films are general strong and adherent, mechanically hard, pinhole free and stable with temperature and time.

The morphology of the films is general rough and that will depend upon the spray conditions. The surface of the substrate gets affected in the spray process and the choice is limited to glass, quartz, ceramics or oxides, nitride or carbide coated substrates[34].

### 1.6.2 Advantages of Spray Pyrolysis Technique

In the current study, how chemical spraying pyrolysis (CSP) used in the preparation of films on the substrates of glass slave (cover glass), and the fact that the films prepared in this way lower quality of films prepared in a manner evaporation vacuum but with fixed characteristics and stability of high and can be used in many applications process, this method is characterized by cheap cost of being compared to the other methods used in devices and techniques are complex, as well as the method (CSP) can be used in the preparation of films with melting high cannot be prepared with other methods, as well as can be prepared films of blending two or more to change rates within the film in a manner (CSP) and prepared in a way that is difficult to evaporation in a vacuum, and the characteristic of this method are [35]:

1- Low technological complexity.
2- Possibility of large area fabrication.
3- Producing a sufficiently high deposition rate.
4- Ease of processibility.
5- Post - deposition heat treatment is not necessary.
6- Possibility mass production usage.
7- There is no need for high purity materials.
8- Thin films prepared by this method are adhesive.

### 1.7 **Literature Survey**

We will conduct a general survey about their findings, the researchers in the study of thin films, as follows:

In (2004) **F. K. Shan et al.** [36] studied ZnO thin films were deposited on Si(100) substrates at different temperatures (100 ~ 600) $^oC$ in the micro-Raman technique was used to characterize the thin films. Raman spectra of the thin films revealed the $E_2$ modes at around (99 and 436) $cm^{-1}$, which indicates that the wurtzite structure is easily formed in the thin films. As a function of growth temperature, greater tensile stress is induced at lower growth temperature.

In (2006) **J.-H. Huang and C.-P. Liu** [37] studied polycrystalline ZnO thin films doped with magnesium was prepared on glass substrates by (RF) magnetron co-sputtering. The chemistry, morphology and optical properties of the resulting thin films with various deposition parameters were investigated. X-ray photoemission spectroscopy results show that a linear composition variation for $Zn_{1-x}Mg_xO$ with amorphous phase can be obtained by varying sputtering power, which results an increasing optical energy gap linearly with (x)% for better light transmission. However, conductivity drops dramatically as soon as Mg is introduced. However, only being exposed to atmosphere would not change conductivity. That the dopant can be applied to improve the properties of ZnO films. The researcher that the amorphous $Zn_{1-x}Mg_xO$ (x about 0.49) film is observed at room temperature due to the amorphous glass, but poor electrical conductivity was obtained due to lack of extrinsic donor sources.

In (2007) **S. S. Hullavarad et al.** [38] described the homo- and hetero-epitaxial growth of hexagonal and cubic $Mg_xZn_{1-x}O$ thin films on lattice matched substrates of ZnO, and MgO. The crystalline quality, composition and epitaxial nature of the alloy films are obtained by X-ray diffraction (XRD) technique. The metal-semiconductor-metal and ultraviolet detectors were fabricated on hexagonal and cubic $Mg_xZn_{1-x}O$ thin films and the leakage current and UV-visible rejection ratio are correlated with the epitaxial relationship between the film and substrates. The researcher found that the study paves the way for the realization of detector improvement methodology for deep UV sensors and provides insight into the understanding of transport properties and individual composition vis- a-vis the crystalline quality. Due to the lattice

matching epitaxy and thermal and optical compatibility between the hexagonal MgZnO film and the ZnO substrate and the cubic MgZnO film and the MgO substrates, the lattice matched heterostructures of h-$Mg_{0.15}Zn_{0.85}O$/ZnO and c-$Mg_{0.9}Zn_{0.1}O$/MgO may be useful for fabrication of hybrid optoelectronic devices.

In (2008) **C. -Y. Tsay et al.** [39] studied polycrystalline thin-films of $Zn_{1-x}Mg_xO$ ($0 < x < 0.36$) have been prepared by a sol-gel method and a spin-coating technique. In this work, the authors investigate the effects of the Mg addition on crystallization, microstructure and optical properties for ZnO thin films. Mg was incorporated into ZnO thin films that were deposited onto glass substrates by a spin coating technique. The results show that addition of Mg-species in ZnO films markedly decreased surface roughness, improved transparency in the visible range and increased resistivity. Among the $Zn_{1-x}Mg_xO$ films investigated in the present study, the $Zn_{0.8}Mg_{0.2}O$ thin film exhibited the best properties, namely single wurtzite phase, an optical transmittance of (94.7)%, an RMS roughness of (1.63) nm. Researchers results that additions of Mg into ZnO thin films not only refine the grain size but also increase the transmittance of thin films. Among the $Zn_{1-x}Mg_xO$ ($0 \le x \le 0.36$) films investigated in the present study, the $Zn_{0.8}Mg_{0.2}O$ film exhibits the best transparency and the highest resistivity. Its average crystallite size is (8.7) nm with its transparency and optical transmittance of (94.7)%.

In (2009) **D. Y. Jiang et al.** [40] studied cubic $Mg_xZn_{1-x}O$ thin films (x=0.7) were grown on quartz substrates by radio frequency magnetron sputtering and a metal-semiconductor–metal structured photodetector was fabricated based on the film. The photodetector exhibited a dominant response peak at about (225) nm with a cutoff wavelength at about (230) nm, which lies in the solar-blind spectrum range (220-280) nm. A shoulder also appeared in the response spectrum at about (265) nm besides the dominant peak, which resulted from the phase separation in the $Mg_{0.70}Zn_{0.30}O$ thin films as revealed by transmission electron microscopy (TEM). The photodetector showed very low dark current (2 pA at 3V bias). The results obtained in this paper

confirm that $Mg_xZn_{1-x}O$ can be a strong candidate for solar blind photodetector applications.

In (2010) **M. Sahal et al.** [41] studied analysis of the chemical composition, structural, and optical properties of Mg-doped ZnO (ZMO) thin films with Mg-content up to (54)% and prepared by the spray pyrolysis technique from acetate precursors. Chemical analysis show that the Mg/Zn ratio incorporated into the films is higher than that present in the starting solution. X-ray diffraction (XRD), Raman scattering, and transmission measurements show that all samples exhibit a single phase wurtzite structure with a transmittance above (70)% in the visible range. Increasing Mg-content leads to an increase of the energy gap from (3.23 in pure ZnO to 3.57) eV in films with (54)% of Mg-content. (EDX) results of the measurements of the films the incorporation of the Mg-content with a higher molar fraction of this element in the layers than that in starting solution. (XRD) and Raman scattering measurements reveal the wurtzite structure of the films and evidence a decrease in the film quality with increase of Mg-content.

In (2010) **S. A. Yousif et al.** [42] studied the electrical properties of the $Zn_{1-x}Mg_xO$ thin film deposited on glass substrate by chemical spray pyrolysis (CSP) technique at a substrate temperature (400)°C for different Mg-content (x=0, 0.1,0.2,0.3, and 0.4) have been studied. All the as-grown $Zn_{1-x}Mg_xO$ films show a resistivity that varied in the range(0.0104-695.894)Ω cm corresponding to the Mg-content (x=0 -0.4) respectively. Hall measurements indicate that the $Zn_{1-x}Mg_xO$ thin films have different conduction type, ZnO pure show n-type conductivity and the films which have concentrations (x =0.1, 0.2, 0.3, and 0.4) show p-type conductivity.

In (2011) **H. Kou et al.** [43] prepared nanosheets of ZnO on porous Si (PS) at different applied potentials by electrodeposition approach. Thus, ZnO grown on (PS) can be used as photoelectric materials due to its larger photoelectric effect compared to Si wafer according to open-circuit potential (OCP) study. Optical energy gap measurements were made on samples using UV-Visible spectrophotometer thus giving an energy gap of (3.35) eV.

In (2012) **S. A. Yousif et al.** [44] studied Mg doped ZnO thin films were deposited on a glass substrate by spray pyrolysis technique at a substrate temperature equal to (400) °C under ambient atmosphere. The energy-dispersive X-ray analysis (EDX) spectra of the $Zn_{1-x}Mg_xO$ thin films reveals that all the films contain the elements (Zn, Mg, O) as expected, indicating formation of the $Zn_{1-x}Mg_xO$ films with high purity. From the (SEM) images the grain size values of the $Zn_{1-x}Mg_xO$ thin films deposited by (CSP) technique are found to be in the ranges of (59-83)nm, (35-59)nm,(47-71)nm,(47-59)nm, and (35-47)nm corresponding to the Mg-contents (x = 0, 0.1,0.2, 0.3, and 0.4) respectively. The (I-V) characteristics of $Zn_{1-x}Mg_xO$/n-Si hetrojunction for dark and illuminated conditions have been investigated. Researcher concluded through his studies that ideality factor values vary from (29.55) to (10.91) with different Mg-contents in the films. The responsivity of $Zn_{1-x}Mg_xO$/n-Si photodetectors for white light has high acceptable values, which indicates that the $Zn_{1-x}Mg_xO$/n-Si photodetectors can be used as detectors in the visible and UV span of the spectrum.

In (2013) **A. Agrawal et al.** [45] studied the structural and optical properties of Mg doped ZnO, Mg (3,5,6,9, and 12)w% thin films prepared by (PLD) technique. The samples are characterized by X-ray diffraction technique and UV-Vis absorption spectroscopy. XRD results reveal the polycrystalline nature of samples with no impurity or secondary phase formation. UV-Vis absorption spectroscopy studies show the blue shift in the optical energy gap subsequent to Mg doping. Researcher concluded from measurements of XRD that all the films so prepared were oriented to the c-axis of wurtzite ZnO structure and no other features related to Mg and MgO were observed. The optical energy gap calculated from UV-Vis absorption spectra of the films increases with the increase of Mg-content.

In (2014) **H. S. Kim et al.** [46] studied single-phase, high band gap energy $Zn_{0.5}Mg_{0.5}O$ films were grown under oxygen pressure, using (PLD) with a $Zn_{0.5}Mg_{0.5}O$ target. Structural characterization studies revealed that the crystal structures of the $Zn_{x-1}Mg_xO$ films could be controlled via changes in the oxygen

pressure. The XRD peak intensity for the hexagonal-ZnMgO (002) plane increased relative to that for the cubic-ZnMgO (111) plane. The corresponding c-axis of the h-ZnMgO lattice constant increased from (5.141 to 5.148) Å, and the a-axis of the c-ZnMgO lattice constant decreased from (4.255 to 4.250) Å. EDX analysis showed that the Mg-content in the mixed-phase ZnMgO films decreased significantly, from (54.25 to 46.96) %. As the oxygen pressure was increased from (100 to 150) mTorr, the absorption edge-shifted from (3.96 to 3.81) eV, this was determined by observing the diffraction pattern beam shape. The single-phase wurtzite ZnMgO films displayed a band gap energy of (4.04) eV and a c-axis lattice constant of (5.1418) Å, which was smaller than that of pure ZnO (5.204)Å. (EDX) analysis indicated that the Mg-content in the ZnMgO film was (46.96)%.

In (2014) **A. A-K. Hussain et al.** [47] studied the effect of Mg doping on structural and optical properties of ZnO prepared by (PLD). The films deposited on glass substrate. The structure and optical properties were characterized by XRD and transmittance measurements. The films grown have a polycrystalline wurtzite structure and high transmission in the UV-Vis (300-900) nm. The optical energy gap of ZnO:Mg thin films could be controlled between (3.2-3.9) eV. The refractive index of ZnO:Mg thin films decreases with Mg doping. The extinction coefficient and the complex dielectric constant were also investigate. The researcher concluded that the films is polycrystalline with hexagonal wurtzite structure with preferential orientation in the (100) direction and intensity decrease with doped Mg. The optical transitions in ZnO are direct and the optical energy gap increases with doping from (3.2 to 3.9) eV.

In (2014) **G. K. Mani et al.** [48] studied the effect of annealing duration on structural, morphological, optical and electrical properties of spray deposited nanostructured ZnO thin films was investigated. Films were deposited on glass substrates at the substrate temperature of (250) $^{o}$C subsequently post annealed at (400) $^{o}$C for (6) h, (12) h and (24) h durations. XRD pattern of the films confirmed the polycrystalline nature with hexagonal wurtzite structure. The gradual grain growth along the c-axis and increase in crystallite size with reference to annealing

duration were confirmed by XRD data. (SEM) of the films revealed the grain growth as an effect of annealing duration. Optical energy gap was found to be decreased from (3.31 to 3.26) eV when the annealing period was increased from (0 to 24) h. Film thickness and electrical conductivity were found to be decreased and increased respectively as the annealing duration was increased.

In (2014) **S. Shanmugan et al.** [49] studied metal Mg doped ZnO thin film was prepared by sol-gel spin coating method on glass substrates followed by annealing at four different temperatures (300 to 450)°C to understand the structural behavior. The structural analysis of Mg doped ZnO thin film was showed the crystal grown in their preferred hexagonal (100) orientation. Noticeable change in surface morphology was observed from the Mg doped ZnO thin film when annealed at the range from (300 to 400)°C. The researcher concluded that the annealing temperature showed immense effect on surface morphology as well as grain size of Mg doped ZnO thin film as compared with bare ZnO thin film. Annealing temperature also influenced the surface morphology irrespective to the doping element and low surface roughness was noticed with Mg doped ZnO film in as grown as well as annealed at (450)°C.

In(2015) **N. Akın et al.**[50] studied $Mg_{0.2}Zn_{0.8}O$ thin films were deposited onto glass and n-Si substrates by radio frequency (RF) magnetron sputtering method under various deposition parameters. Structural, morphological and optical properties of the films were investigated by XRD, atomic force microscope and UV-Vis spectrometer. Then, UV sensing of the fabricated $Mg_{0.2}Zn_{0.8}O$ thin films-based sensors was explored by using current-voltage (I-V) characteristics. The results showed that our sensors were sensitive in the UV region of the electromagnetic spectrum. This achieved UV sensor might probably be used in flexible device application, and this also opens a new way for fabricating inexpensive flexible devices.

In(2015) **R. Singh and A. A. Koser** [51] studied ZnO is one of the most widely used inorganic material since it has a wide energy gap of (3.37) eV and high mechanical and thermal stability. It belongs to (II-VI) semiconductor group. Doping with selective elements offers an effective method to enhance and control the optical

and electrical properties of ZnO nanostructures, which is crucial for its practical applications. Mg doped ZnO have significant interests owing to their unique optical, piezoelectrical and electrical properties. In this paper, they have reported the synthesis of ZnO and Mg-doped ZnO nanoparticles using thioglycerol as a capping agent by using chemical precipitation method. The characterization of ZnO nanoparticles and Mg doped ZnO nanoparticles using UV spectrophotometer revealed a significant change in property due to doping and they observed the shift in the wavelength, this patent the change in the energy gap as well. The particle size was calculated using effective mass approximation method which comes out to be (3.77) nm for ZnO nanoparticles and(4.48) nm for Mg doped ZnO nanoparticles. Researcher concluded that particle size of ZnO and MgZnO was found to be (3.77) nm and (4.48) nm. The optical energy gap of doped and undoped nanoparticles was studied and it is found that the energy gap of doped ZnO was shifted slightly towards longer wavelength region.

In(2015) **J. Gao et al.** [52] studied structural properties of materials, in particular the composition dependence on the lattice constant and the energy gap is found to be linear. The a-axis length in the lattice gradually increases, while the c-axis length decreases with the increase in Mg doping concentration. The lattice parameters of the $Mg_xZn_{1-x}O$ ternary alloys are consistent with experimental data and other theoretical results. They found in the conduction band portion, the Mg (2p 2s) states are moved to high energy region as the Mg-content increases, so the energy gap increases. Concluded researcher the calculated results show the calculated lattice constants scale linearly with composition.

## 1.8 Aims of the Work

The aim of this work, is to prepare p-$Mg_xZnO_{1-x}$ films nanostructure by using chemical spray pyrolysis (CSP) technique .Then study their structural characteristics, optical, electrical, and sensing. Thus identify areas of their practical applications for the manufacture of photodetectors and gaseous sensors.

## 2.1 Introduction

This chapter gives a general description of the theoretical part containing the characteristics. Structural, Raman shift, optical and electrical, photoconductive detector, and gas sensor of $Mg_xZnO_{1-x}$/n-Si heterojunction. Finally, this chapter provides a theoretical overview including all relations, scientific explanations, and the equations that are used in this dissertation.

## 2.2 X-Ray Diffraction (XRD)

X-ray diffraction peaks consist of interference construction monochrome rays reflected from any position of lattice levels at certain angles. It can calculate the distance interfaces between the levels of the diffraction angle at a certain peak by using (Bragg's law) [53].

$$n \lambda = 2d_{hkl} \sin\theta_B \qquad (2\text{-}1)$$

Where n integer number that represents interference degree (n=1,2, 3,…), λ is the wavelength of the X-ray (1.54) Å [53] , $d_{hkl}$ is the spacing between diffracting planes and $\theta_B$ is the Bragg's angle. Normally XRD is used to calculate different parameters which could be used to clarify the studies of the deposited films such as:

### 2.2.1 Lattice Constants

The many crystal phases available in transparent conductive oxides (TCOs), hexagonal structure is the dominant phase in ZnO material, hexagonal phase is characterized by determining the (a and c) are lattice constants from X-ray patterns and by using the following formula [54,55]:

$$\frac{1}{d_{hkl}^2} = \frac{4}{3}\left(\frac{h^2+hk+k^2}{a^2}\right) + \frac{l^2}{c^2} \qquad (2\text{-}2)$$

Where (hkl) are Miller indices ,the a-parameter is obtained from the plane (h00), while the plane (00l) is used to obtain c-parameter. In the case of cubic diamond phase such as

crystalline silicon, the a-lattice constant can be obtained from [56]:

$$\frac{1}{d_{hkl}^2} = \left(\frac{h^2+k^2+l^2}{a^2}\right) \qquad (2\text{-}3)$$

### 2.2.2 Full Width at Half Maximum

The β of the preferred orientation (peak) could be measured, since it is equal to the width of the line profile (in radian) at the half of the maximum intensity.

### 2.2.3 Average Crystallite Size

The single line method is one of the several line profile analysis methods based on a Voigt function to determine the size–strain parameters (microstrains and crystallite sizes). The reason behind the peak shifting was the change of stress, firstly due to the increase in temperature additionally due to the increase in Mg-concentration. The lower boundary of the crystallite size $D_s$ of the films was estimated using the full width at half maximum (FWHM) of (002). The average crystallite size $D_s$, which can be estimated using the Debye Scherer's formula [56].

$$D_s = \frac{k\,\lambda}{\beta\ \cos(\theta)} \qquad (2\text{-}4)$$

Where k=0.94 is the shape factor, λ is the wavelength of incident X-ray, β is the FWHM measured in radians and θ is the Braggs angle of diffraction peak. The FWHM of the peak corresponds to (002) plane was narrowed with increasing temperature, indicating improvement in crystallinity [56].

### 2.2.4 Microstrains

The microstrains are caused during the growth of thin films, and will be raised from stretching or compression in the lattice to make a deviation in the c-lattice constant of the hexagonal structure of the ASTM values. So the strain broadening is caused by varying displacements of the atoms with respect to their reference lattice position. This strain can be calculated from the formula [57]:

$$S = \frac{\beta\ \cos(\theta)}{4} \qquad (2\text{-}5)$$

### 2.2.5 Dislocation Density

Dislocations ($\delta_D$) are an imperfection in a crystal associated with misregistry of the lattice in one part of the crystal with respect to another part. Unlike vacancies and interstitial atoms, dislocations are not equilibrium imperfections, i.e. thermodynamic considerations are insufficient to account for their existence in the observed densities. In fact, the growth mechanism involving dislocation is a matter of importance. In the present study, the dislocation density ($\delta_D$) can be calculated using the following relation [54].

$$\delta_D = \frac{1}{D_s^2} \qquad (2\text{-}6)$$

### 2.2.6 Number of Layers

The number of crystalline layers ($N_\ell$) which could be calculated due to the percolation theory, and it depends on the film thickness (t) as the relation [58]:

$$N_\ell = \frac{t}{D_s} \qquad (2\text{-}7)$$

## 2.3 Field Emission Scanning Electron Microscopy

FESEM is one of the widely instruments used in material research laboratories. In this technique, electrons are used instead of light waves to see the microstructure of surface of a specimen. However since electrons are excited to high energy (KeV), so wavelength of electron waves are quite small and resolution is quite high. Applications of FESEM include semiconductor device cross section analyses for gate widths, gate oxides, film thicknesses, construction details, small contamination feature geometry, and elemental composition measurement. Compared with convention scanning electron microscopy SEM, field emission scanning electron microscopy(FESEM) produces clearer, less electrostatically distorted images with spatial resolution down to (1.5)nm (3 to 6) times better[59].

## 2.4 Atomic Force Microscopy

Atomic force microscopy AFM is commonly used to characterize surface topography of given samples. Technologies acting the electronics, biological, chemical, and automotive industries use the AFM to solve processing and materials

problems. The materials being investigated include thin and thick coatings, semiconductors, ceramics, metals, micromechanical properties of biological samples, nucleic acids, polymers and biomaterials, to name a few. The AFM has made it possible to obtain 3-D images of surfaces down to the atomic scale as well as measure forces on a nano-newton scale. The working components of the AFM are continually evolving [60]. The surface morphology of spin coated metal doped ZnO thin film on glass substrates are recorded by atomic force microscopy.

## 2.5 Raman Spectroscopy

Raman spectroscopy is a technique that investigates a sub-category of a material's vibration conditions using monochromatic light. The activities of this technique are represented in its ability to convey the information about the characteristic vibrations of the material, both optical and electronic. During irradiation, the spectrum of the scattered radiation is measured at (90) deg. with an appropriate spectrometer. The intensities of the Raman lines are (1)% of the intensity of the source, which could be Stokes scattering. The emitted radiation produces three types of scattering signal: the first two types are Stokes and anti-Stokes scattering that represent less than (1)% of the scattering radiation, while the third type is Rayleigh scattering as shown in fig. 2.1, which accounts for more than (99)%.

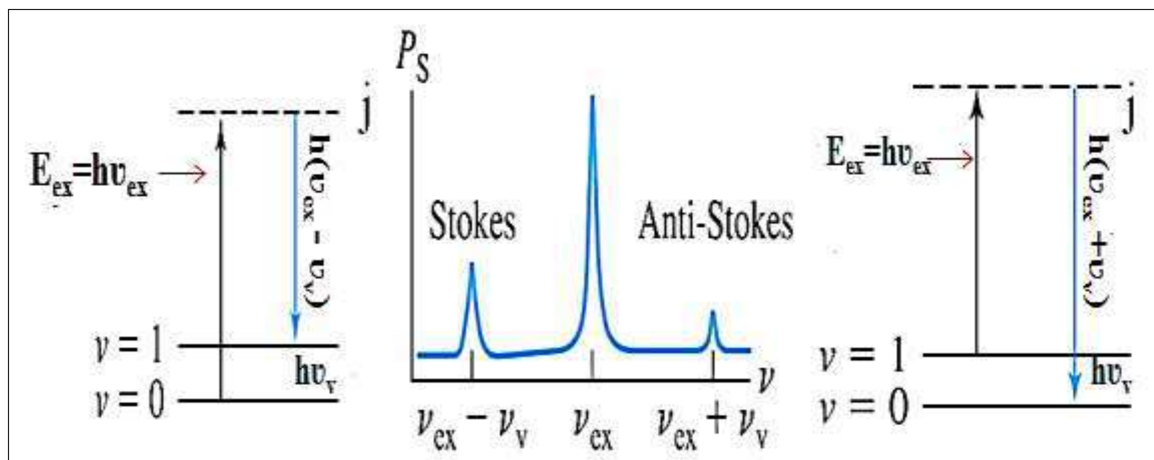


Fig. 2.1: Schematic of the Stokes and anti-Stokes Transition with a Raman Shift [61].

The first type refers to the indicator for Raman spectroscopy, but not all of it because the anti-Stokes lines are appreciably less intense that the corresponding

Stokes lines . As shown in fig. 2.2. Thus, only the Stokes part of the spectrum is generally used. The magnitude of the Raman shifts is independent of the excitation wavelength. The Raman spectrum is represented by the wavenumber shift Δυ, which is defined as the difference in wavenumbers ($cm^{-1}$) between the observed radiation and that of the source. The Stokes and anti-Stokes types are different from the Rayleigh radiation in terms of their frequencies corresponding to ±ΔE, the energy of the first vibrational level of the ground state. If the bond was infrared active, the energy of its absorption would also be ΔE.

Thus, the Raman frequency shift and the infrared absorption peak frequency is identical [61]. Rayleigh scattering has a considerably higher probability of occurrence than Raman because the most probable event is the energy transfer to molecules in the ground state and reemission by the return of these molecules to the ground state (>99%). The relative population of the two Stokes emissions is much favored over anti-Stokes. The ratio of anti-Stokes to Stokes intensities increases with temperature because a larger fraction of the molecules is in the first vibrationally excited state under these circumstances.

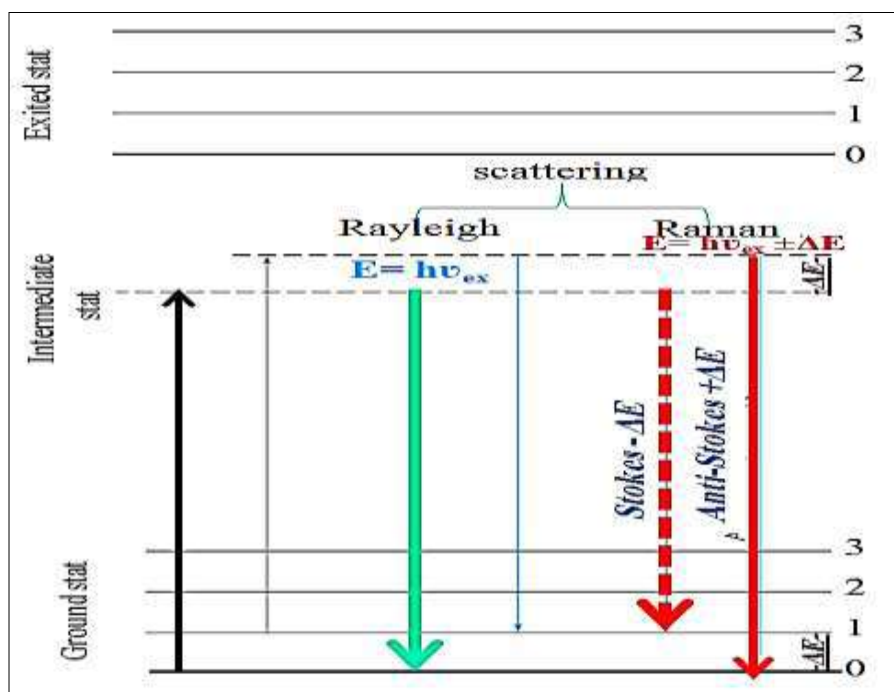


Fig.2.2: Schematic Diagram Showing the Types of Transition of the Electrons and the Rayleigh and Raman Scattering [61].

The most important property of Raman spectroscopy is that the energy shifts observed in a Raman experiment should be identical to the energies of its infrared absorption bands, provided that the vibrational activities involved are active with both infrared absorption and Raman scattering [62]. The differences between a Raman spectrum and an infrared spectrum depend on the real conditions between them, that is, the dipole moment. Infrared absorption requires that a vibrational mode of the molecule has a change in dipole moment or the charge distribution associated with it. Scattering involves a momentary distortion of the electrons distributed around a bond in a molecule, followed by reemission of the radiation as the bond returns to its normal state.

In its distorted form, the molecule is temporarily polarized, which momentarily develops an induced dipole that disappears upon relaxation and reemission. The Raman activity of a given vibrational mode may differ markedly from its infrared activity. The intensity of the Raman peak depends in a complex way on the polarizability of the molecule, the intensity of the source, and the concentration of the active group. The power of the Raman emission increases with the fourth power of the frequency of the source, however, advantage can rarely be taken of this relationship because of the probability that ultraviolet irradiation will cause decomposition by the light. Raman intensities are usually directly proportional to the concentration of the active species. Polarization is a property of a beam of radiation and describes the plane in which the radiation vibrates. Raman spectra is excited by plane-polarized radiation. The scattered radiation is found to be polarized to various degrees depending on the type of vibration responsible for the scattering [63].

### 2.5.1 Raman Spectroscopy of ZnO Thin Films

ZnO has the wurtzite structure with $C_{6V}$ symmetry. It is a polar uniaxial crystal and it has no centre of inversion-therefore it has piezoelectric properties. The wurtzite lattice has (4) atoms per unit cell. The Raman active zone centre phonon vibrations predicted are: one $A_1$ mode, one $E_1$ mode and two $E_2$ modes, (group theory also predicts two $B_1$ modes but these are silent). The infrared active vibrations are the $A_1$

and $E_1$ modes. In wurtzite ZnO long range electrostatic forces dominate over the short range interatomic forces. This leads to a split into longitudinal and transverse components of the phonon normal modes that are infrared active i.e. the $A_1$ and $E_1$ modes will be split. There will be $A_1$(TO), $A_1$ (LO), $E_1$(TO) and $E_1$(LO) vibrational modes in the Raman spectrum of ZnO as well as the two $E_2$ modes (TO=Transverse Optical and LO=Longitudinal Optical). Many experiments have been carried out to distinguish which peak values correspond to which normal modes [64]. To do this, the incident radiation must be polarized, the direction of propagation of the incident light must be controlled and the scattered radiation must be analyzed.

### 2.5.2 Impurities and Defects

The translational symmetry of a crystal is what defines a phonon. If impurities or defects break this translational symmetry, new modes can occur. Localized modes occur when their frequency is too large to propagate through the crystal like a normal phonon . These modes can be known as band modes (non-localized) when the defect or impurity atom is heavier than the lattice atoms surrounding it. In a diatomic crystal, as in the case of ZnO and $Mg_xZnO_{1-x}$ for small ( x)%, if a lighter atom replaces the heavier atom, localized modes and gap modes occur. Localized modes are ones whose frequencies occur higher than the perfect lattice frequencies i.e. all acoustic and optical modes. Gap modes have frequencies between bands of allowed modes ( i.e. between the acoustic and optical modes in ZnO). Band modes occur within bands of perfect lattice frequencies i.e. between the TA and LA modes or between TO and LO modes [64].

## 2.6 Optical Properties

The optical properties of a semiconductor are related to intrinsic effect. Based on the intrinsic location of the top of the valence band (V.B) and bottom of the conduction band (C.B) in the band structure, the electron-hole pair generation occurs directly or indirectly. The ZnO thin film is a wide direct energy gap compound

semiconductor. It is highly transparent in the visible range (depends on the deposition technique and thickness). The n-type conductivity is due to the lack of oxygen and an excess of Zinc [65].

### 2.6.1 Optical Absorption and Absorption Edge

The fundamental absorption is the most important absorption process which involves the transition of electrons from the valence to the conduction band, which manifests itself by a rapid rise in absorption and this can be used to determine the energy gap of the semiconductor [66]. The semiconductor absorbs photon from the incident beam, the absorption depends on the photon energy (hυ), where h is plank's constant, υ is the incident photon frequency, the absorption is associated with the electronic transition between the (V.B) and the (C.B) in the material starting at the absorption edge which corresponds to minimum energy difference ($E_g$) between the lowest minimum of the (C.B) and the highest maximum of the (V.B) [67]. If the photon energy (hυ) is equal or more than energy gap ($E_g$) then, the photon can interact with a valence electron, elevates the electron into the (C.B) and creates an electron-hole pair. The maximum wavelength ($\lambda_c$) of the incident photon which creates the electron-hole pair is defined as [68].

$$\lambda(\mu m) = \frac{hc}{E_g} = \frac{1.24}{E_g(eV)} \qquad (2\text{-}8)$$

The intensity of the photon flux decreases exponentially with distance through the semiconductor according to the following equation [69].

$$I = I_o \exp(-\alpha t) \qquad (2\text{-}9)$$

Where $I_o$, I are the incident and the transmitted photon intensity respectively and $\alpha$ is the absorption coefficient is given in equation (2-10), which is defined as the relative number of the photons absorbed per unit distance of semiconductor, and t is the thickness of the film [70].

$$\alpha = 2.303\frac{A}{t} \qquad (2\text{-}10)$$

Where A is the absorbance and t is the sample thickness.

### 2.6.2 Direct Transitions

The direct transition in general occurs between top of valence band and bottom of conduction band (vertical transition) at the same wave vector (Δk=0) for conservation of momentum. The allowed direct transition refers to that transition which occurs between top of the valence band and bottom of the conduction band when the change in the wave vector equal to zero (Δk=0). This transition is described by the following relation [71].

$$\alpha h\nu = B' \left(h\nu - E_g\right)^{1/2} \qquad (2\text{-}11)$$

Where $B'$ is inversely proportional to amorphusity, $h\nu$ is the photon energy, $E_g$ is the band gap. If the transition occurs also between states of the same wave vector, but the wave vector does not equal to zero, the transition is called forbidden direct transition, it obeys the following relation [72].

$$\alpha h\nu = B' \left(h\nu - E_g\right)^{3/2} \qquad (2\text{-}12)$$

### 2.6.3 Optical Constants

The optical constants are very important parameters because they describe the optical behavior of the materials. The absorption coefficient of the material is a very strong function of the photon energy and band gap energy. Optical constants included refractive index (n), extinction coefficient ($k_o$), and real ($\varepsilon_r$) and imaginary parts ($\varepsilon_i$) of dielectric constant. The complex refractive index ($n_c$) is defined as [73].

$$n_c = n - ik_o \qquad (2\text{-}13)$$

And it is related to the velocity of propagation v, and light velocity c by:

$$v = \frac{c}{n_c} \qquad (2\text{-}14)$$

The refractive index value can be calculated from the formula [74].

$$n = \left(\frac{4R_e}{(R_e-1)^2} - k_o^2\right)^{1/2} - \frac{(R_e+1)}{(R_e-1)} \qquad (2\text{-}15)$$

Where $R_e$ is the reflectance, and can be expressed by the relation [70].

$$R_e = \frac{(n-1)^2 + k_o^2}{(n+1)^2 + k_o^2} \qquad (2\text{-}16)$$

The extinction coefficient, which is related to the exponential decay of the wave as it passes through the medium, is defined as [74].

$$k_o = \frac{\alpha\lambda}{4\pi} \qquad (2\text{-}17)$$

The real and imaginary part of dielectric constant can be calculated by using the following equation [71].

$$(n - ik)^2 = \varepsilon_r - i\varepsilon_i \qquad (2\text{-}18)$$

Where

$$\varepsilon_r = n^2 - k_o^2 \qquad (2\text{-}19)$$

and

$$\varepsilon_i = 2nk \qquad (2\text{-}20)$$

## 2.7 Electrical Properties of ZnO Thin Film

ZnO thin films with various electrical properties have been fabricated:

a- "Stoichiometrically" doped ZnO layers. The oxygen partial pressure impacts point defect formation and the ZnO can be made naturally $n_e$- conducting with typical electron density $n_e = (10^{16}\text{-}10^{18})\ cm^{-3}$ [75].

b- Unintentionally doped ZnO layers, due to Al diffusing from the sapphire substrate. The electron density is typically $n_e=(10^{16})\ cm^{-3}$ with an activation energy $E_a= (65)$meV [76].

c- "Clean" ZnO layers with a MgO buffer layer between ZnO and $Al_2O_3$.This buffer reduces the diffusion of Al. Semi-insulating behavior and a low electron concentration of $n_e$ ($\sim 10^{14}$) $cm^{-3}$ can be achieved at the suitable oxygen partial pressure of (0.01- 0.1) mbar [77].

d- Intentionally doped ZnO layers with Al (and electron) concentration in excess of (1020) $cm^{-3}$. Due to the formation of an impurity band, the donor binding energy decreases with increasing doping and vanishes at about $(10^{19})\ cm^{-3}$ [78].

e- Compensated ZnO layers, obtained by growth of ZnO with a $N_2O$ atmosphere $n_e = (10^{16}\text{-}10^{19})\ cm^{-3}$ [79].

f- Co-doped, compensated ZnO layers which are grown with simultaneous Ga and N (PLD) target and $N_2O$ atmosphere. Semi-insulating doping from $Ga_2O_3$ with a behavior with low electron concentration $n_e = (10^{14})\ cm^{-3}$ is achieved for a variety of $N_2O$ pressures and Ga concentration up to$(10^{19})\ cm^{-3}$. We achieve homogeneous ZnO layers on 2 in sapphire substrates with a mobility of $\mu = (155)\ cm^2/V.s$ at room temperature for layers of type (a) with $n_e$ around $(10^{17})\ cm^{-3}$. The mobility is limited, compared to bulk material with $\mu \sim (220)\ cm^2/V.s$, due to scattering at charged defects. The electrical properties depend upon the nature of semiconductors, if they are pure or doped and crystalline or amorphous [80].

### 2.7.1 The Direct Continuous Electrical Conductivity

Electrical conductivity $\sigma$ is defined as the proportional factor between the current density J and the electric field E, and it is given by Ohm's law [81].

$$J = \sigma E \qquad (2\text{-}21)$$

Where

$$\sigma = n_e q \mu \qquad (2\text{-}22)$$

or

$$\sigma = \frac{n_e q^2 \tau}{m^*} \qquad (2\text{-}23)$$

Where $\mu$ is the mobility, $\tau$ is the carrier's lifetime, $n_e$ is the carrier's concentration, $m^*$ is the effective mass of the carrier and q is the electron charge. In semiconductors the relation between the current density and electric field is given by [81].

$$J = q(n_e \mu_n + p\mu_p) \qquad (2\text{-}24)$$

Where n and p are the electron and hole concentration and $\mu_n$ and $\mu_p$ are the mobility of electron and hole respectively, where:

$$\mu = \frac{V_d}{E} \qquad (2\text{-}25)$$

Where $V_d$ is the drift velocity. Then the relation between the conductivity and electron - hole concentration is.

$$\sigma = q(n_e\mu_n + p\mu_p) \qquad (2\text{-}26)$$

In practice, the material will be either n-type or p-type, and then equation (2-26) will be:

$$\sigma_n = qn_e\mu_n \quad \text{for n-type} \qquad (2\text{-}27)$$

$$\sigma_p = qn_p\mu_p \quad \text{for p-type} \qquad (2\text{-}28)$$

For most cases of semiconductor the following equation gives the change of the electrical conductivity with temperature [82].

$$\sigma = \sigma_o \exp\left(\frac{-E_a}{K_B T}\right) \qquad (2\text{-}29)$$

Where $\sigma_o$ is the minimum electrical conductivity at 0K, $E_a$ is the activation energy which corresponds to ($E_g/2$) for intrinsic conduction, T is the temperature and $K_B$ is the Boltzmann's constant [82]. The resistivity ρ of the films is calculated by using the following equation.

$$\rho = \frac{RA_r}{\ell} \qquad (2\text{-}30)$$

Where R is the film resistance , $A_r$ is the cross section area of the film, and $\ell$ is the distance between the electrodes. The conductivity of the film was determined from the relation:

$$\sigma_{D.C} = \frac{1}{\rho} \qquad (2\text{-}31)$$

The activation energy could be calculated from the plot of $\ln\sigma_{D.C}$ versus 1000/T according to equation (2-29).

### 2.7.2 Hall Effect

When a conductor is placed in a magnetic field and a current passed through it an electric field will be produced, the direction of which is normal to both the current and magnetic field directions. This phenomenon, discovered by E.T. Hall in 1879, is known as the Hall effect [83].

$$R_H = \frac{V_H}{I_x} \cdot \frac{t}{B_Z} \qquad (2\text{-}32)$$

The Van der Pauw method which was first propounded by L.J. Van der Pauw in 1958 is often used to measure the Hall effect, which characterizes a sample of semiconductor material and can be successfully completed with a current source, voltmeter, and a magnet. From the measurements made, the following properties of the material can be calculated [84]. The doping type (i.e. if it is a p-type or n-type) material.

- The sheet carrier density of the majority carrier (the number of majority carriers per unit area). From this, the density of the semiconductor, often known as the doping level, can be found for a sample with a given thickness.
- The mobility of the majority carrier.

In order to use the Van der Pauw method, the sample thickness must be much less than the width and length of the sample. In order to reduce errors in the calculations, it is preferable that the sample is symmetrical. There must also be no isolated holes within the sample for a simple metal where there is only one type of Hall voltage $V_H$ is given by:

$$V_H = \frac{-iB/t}{n_e q} \qquad (2\text{-}33)$$

Where B is magnetic field, the Hall coefficient is defined as:

$$R_H = \frac{E_y}{j_x B} = \frac{V_H}{iB/t} = -\frac{1}{n.q} \qquad (2\text{-}34)$$

The simple formula for the Hall coefficient given above becomes more complex in semiconductors where the carriers are generally both electronic and holes which may be present in different concentrations and have different motilities for moderate magnetic fields the Hall coefficient is:

$$R_H = \frac{-n_H \mu_e^2 + p_H \mu_h^2}{q(n_H \mu_e + p_H \mu_h)^2} \qquad (2\text{-}35)$$

For large applied fields the simpler expression analogous to that for a single carrier type holds [85].

$$R_H = \frac{1}{(p_H - n_H) q} \qquad (2\text{-}36)$$

Hall mobility $\mu_H$ could be calculated from the product of the conductivity σ, and the Hall coefficient according to the equation.

$$\mu_H = \sigma R_H \qquad (2\text{-}37)$$

## 2.8 Theory of Heterojunction

Heterojunctions play an important role in semiconductor devices such as solar cells, light-emitter diode, photo detector, solid state laser and integrated circuits [86].

A heterojunction is a junction formed at the interface of two semiconductors which are assumed to have different energy gaps ($E_g$), different permittivity's ($\varepsilon_s$), different work functions ($\Phi_m$) and different electron affinities ($\chi$). Work function and electron affinity are defined as the energy required to remove an electron from the Fermi level ($E_F$) and from the bottom of the conduction band ($E_C$) respectively, to a position just outside the material (vacuum level), as shown in fig.2.10[87]. In principle it is possible to construct heterojunctions in which both semiconductors have the same energy gap. However most studies of heterojunctions have involved two semiconductors comprised of different values of energy gaps[83] .

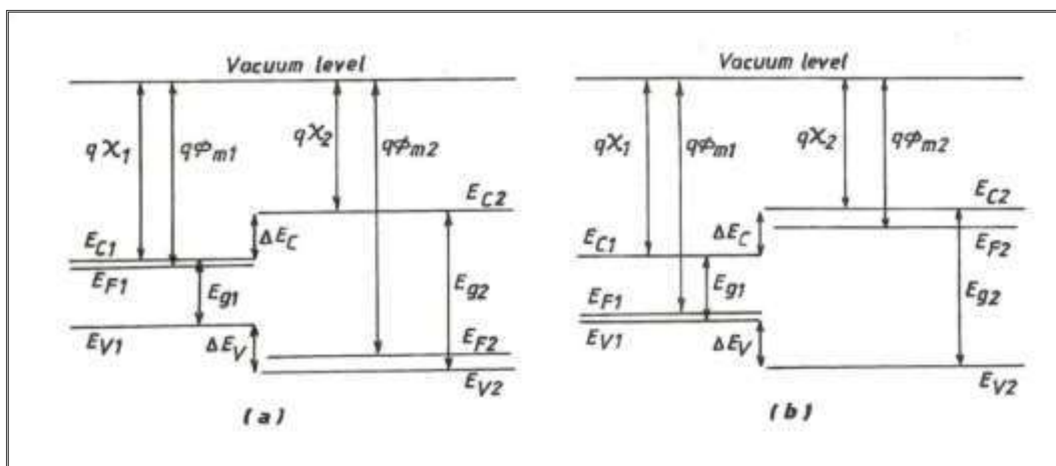


Fig.2.3: Energy-Band for two Isolated Semiconductors of Opposite Types and Different $E_g$ (a) the Smaller Energy Gap is n-type and (b) the Bigger Energy Gap is p-type [87].

### 2.8.1 Band Profile of Heterojunction

When two semiconductors contact to form a heterojunction one with a narrow-energy gap material and the other wide-energy gap material, the forbidden energy gap of the wide-gap material completely overlaps the energy gap of the narrow-gap

material, then this case is called straddling. The other possibilities are called staggered and broken gap as shown in fig.2.4 [83].

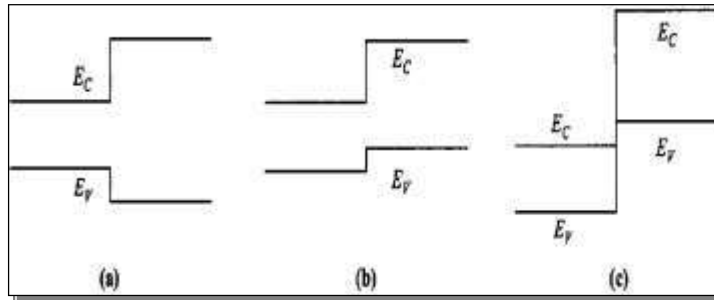


Fig. 2.4: Classification of heterojunctions as
(a) straddling, (b) staggered, and (c) broken-gap [88].

According to their band alignment, heterojunctions can be classified into three groups as shown in fig. 2.4:

- Type-1 or straddling heterojunction.
- Type-2 or staggered heterojunction.
- Type-3 or broken-gap heterojunction.

### 2.8.2 Lattice Mismatch:

Degree of perfection of fit to a great extent and the crystalline structure of the grown layer depending on the lattice match of two materials. The lattice match is important because any lattice mismatch can introduce dislocations resulting in interface states [87]. The lattice mismatch between two semiconductor having lattice constant $(a_2)$ and $(a_1)$ is defined as.

$$\Delta = \frac{2|a_2 - a_1|}{a_2 + a_1} \times 100\% \qquad (2\text{-}38)$$

Where $\Delta$ *is* lattice mismatch, severe lattice mismatch will cause dislocations at the interface and results in electrical defects such as interface traps.

### 2.8.3 Thermal Mismatch:

Another factor which influences the properties of grown heteroepitaxial layers is thermal mismatch between materials. Even when two materials have essentially the same lattice constant at room temperature, a mismatch may occur at higher temperature when they have different coefficient of thermal expansion. This means

that dislocation may be introduced during cooling from elevated temperatures because a good lattice match is unlikely to exist over a wide range of temperature. In extreme cases this thermal mismatch may even result in cracking or peeling off of grown layers[87].

### 2.8.4 Interdiffusion

Apart from thermal mismatch, an effect of so-called interdiffusion is also present at the interface of those heterojunctions which are fabrication at elevated temperature. This interdiffusion, which especially takes place in the case of heterojunctions formed by two compound semiconductors, is the diffusion of the composing elements of the semiconductors and their dopants at both sides of the interface. This may change the abrupt nature of the heterojunction and/or induce Heterojunction can also be classified into abrupt or dislocations at the interface[87]. graded junction according to the distance during which the transition of charge from one material to the other is completed near the interface. For the abrupt case, the transition occurs within a few atomic distances (1) µm, while graded takes place over distances of the order of several diffusion lengths .The energy band profile has the of staggered gap [86]. case

### 2.8.5 Electrical Properties of Hererojunction

For knowledge of efficient heterojunction, it must study its properties and represented with electrical characteristics of capacitance - voltage (C-V) characteristics and current - voltage (I-V) which gives an idea of the type of factory diode [86] .

#### 2.8.5.1 Capacitance -Voltage Characteristics

The measurement of the junction capacitance (C=dQ/dV) as a function of reverse bias is often used as a powerful experimental technique for the analysis of the depletion region potential and the charge distribution in a heterojunction.The expression of the capacitance per unit area under reverse bias voltage can be written as [89].

$$C = \frac{dq}{dV} = \frac{\varepsilon_s}{w} \quad (2\text{-}39)$$

Where $\varepsilon_s$ is the semiconductor permittivity of the two semiconductor materials, V applied voltage, w depletion width layer. The cross point ($1/C^2=0$) of the ($1/C^2$-V) curve represents the built-in potential of the heterojunction, the charge-carrier density $N_d$ and width of the depletion layer for both devices are calculated by the following equations [89].

$$N_d = \frac{2}{q\varepsilon_s}[1/d(1/C^2)/dV] \quad (2\text{-}40)$$

Where $q$ charge of electron, and it equals ($1.6\times10^{-19}$) C.

$$w = \left[\frac{2\varepsilon_s V_{bi}}{qN_d}\right]^{1/2} \quad (2\text{-}41)$$

Where $V_{bi}$ built-in potential, is calculated by the following equation.

$$V_{bi} = V_{a+} \frac{kT}{q} \quad (2\text{-}42)$$

Where $V_a$ is the applied voltage.

#### 2.8.5.2 Dark Current–Voltage Characteristics

Dark (I-V) characteristics have been measured. These measurements usually provide a valuable source of information about the junction properties, such as the rectification ratio ($R_F$), the ratio of the forward current to the reverse current at a certain applied voltage is defined as the rectification factor, tunneling factor ($\gamma$), the barrier height, the reverse saturation current density and the ideality factor ($\eta$) [90]. The total dark current of the heterojunctions can be represented as a sum of several components such as generation-recombination current, diffusion current, tunneling current, surface leakage current, and emission current [91]. If generation-recombination and diffusion mechanisms are dominant, then the dark current $I_d$obeys the following formula [92].

$$I_d = I_s[e^{-qV/\eta k_B T} - 1] \quad (2\text{-}43)$$

Where $I_s$ is the reverse saturation current and is given as:

$$I_s = A^* T^2 e^{-q\Phi_B/\eta k_B T} \quad (2\text{-}44)$$

Where $A^*$ is Richardson constant, V is the applied voltage, $\Phi_B$ is barrier height, and T is the temperature in Kelvin. The η ideality factor is calculated from the (I-V) characteristics by using the following equation [93].

$$\eta = \frac{q}{k_B T} \frac{V}{ln\frac{I_s}{I}} \quad (2\text{-}45)$$

The value of the η is determined from the slope of the straight line region of the forward bias logarithm of the current as a function of the applied voltage [90]. The current is due to tunneling that dominates across the junction and it could be represented by the expression [87].

$$I = I_s e^{\gamma V} \quad (2\text{-}46)$$

This expression is justified for tunneling–recombination mechanism. The reverse bias characteristics of these heterojunction show a linear variation at low reverse voltage.

#### 2.8.5.3 Under Illumination Current–Voltage Characteristics

Optoelectronic properties of photodetectors were studied under illumination , it can be classified into two groups, one which deals with the generation of photocurrent due to the absorption of photons while the other deals with the emission of photons as a result of electronic excitation in photodetectors. There are two important absorption processes which often have an influence on the photoelectric properties of photodetectors: the creation of free electrons or holes (i.e. photo-excitation of an impurity or interface state) and of free electron - hole pairs (i.e. electron transition from the valence band into the conduction band). The free carriers generated by these processes at the interface or within a diffusion length from it, in the two semiconductors forming a photodetector, give rise to photocurrents in the photodetector [89].

## 2.9 Photocurrent Gain

The photocurrent gain (PG) of a detector is defined as the number of charge carriers flowing between the two contact electrodes of a detector per second for each photon absorbed per second that is.

$$G = \frac{\tau}{t_r} \qquad (2\text{-}47)$$

Where $\tau$ is the carrier lifetime , $t_r$ is the transit time , it is express by [94].

$$t_r = \frac{\ell^2}{\mu . V_a} \qquad (2\text{-}48)$$

Where $\mu$ is the majority carrier mobility, and $V_a$ is the bias voltage applied to the sample. That of important parameters in photoconductor is gain (is a ratio between photocurrent $I_{ph}$ to the dark current $I_d$). This characterization was adopted to determine the gain as follows [95].

$$G = \frac{I_{ph}}{I_d} \qquad (2\text{-}49)$$

Where $I_{ph}$ is the photocurrent, $I_d$ is the dark current. Also, it can be determed the photosensitivity as follows [67].

$$\text{photosensitivity} = \frac{I_{ph} - I_d}{I_{ph}} \qquad (2\text{-}50)$$

**2.10 Photon Detectors**

Photon detectors are solid- state devices that operate under the influence of photon effects. The photon detectors essentially measure the rate at which quanta are absorbance , thus they respond only to those photon of short wavelength; therefore, their response at any wavelength is proportional to the rate at which photons of that wavelength are absorbed. In photon detectors, the radiation is absorbed directly by the electronic system to cause changes in the electrical properties. Photon detectors have small sizes, minimum noise, low biasing voltage, high sensitivity, high reliability, and fast response time. Therefore, they are very useful in optical-fiber communications systems. Basically, if a photon of sufficient energy excites an electron from a non-conducting state into a conducting state, the photoexcited electron will generate current or voltage in the detector. The electronic excitation

requires that the incident photon energy must be equal to or greater than the electronic excitation energy. In other words, the excitation condition is [94].

$$E_{exc} \leq h\upsilon \quad (2\text{-}51)$$

Or

$$E_{exc} \leq \frac{1.24}{\lambda_0} \quad (2\text{-}52)$$

Where $E_{exc}$ is the electronic excitation energy in (eV), $\lambda_0$ is the free space wavelength in micrometers. Most photon detectors have a detectivity that is one or two orders of magnitude greater than thermal detectors, and the response time of photon detectors is very short due to direct interaction between the incident photons and the electrons of the detector material. This interaction is called photo effect [94]. Photon detectors include photoconductive (PC), photovoltaic (PV) and photo emissive detectors. The present study specializes in photoconductive detectors and therefore, they will be concentrated upon it in next part.

### 2.10.1 Photoconductive Detectors

Since the nineteenth century, it has been known that certain materials have the power of changing their resistance on exposure to light. Such materials are known as photoconductors. They represent the first type of semiconductor photon detector. The photoconductive detector consists of a single crystal of semiconductor material of two Ohmic contacts as shown in fig.2.5, and a voltage applied between them. The semiconductor is conducted, and therefore some current flows even without light shining on the material (dark current) [94].

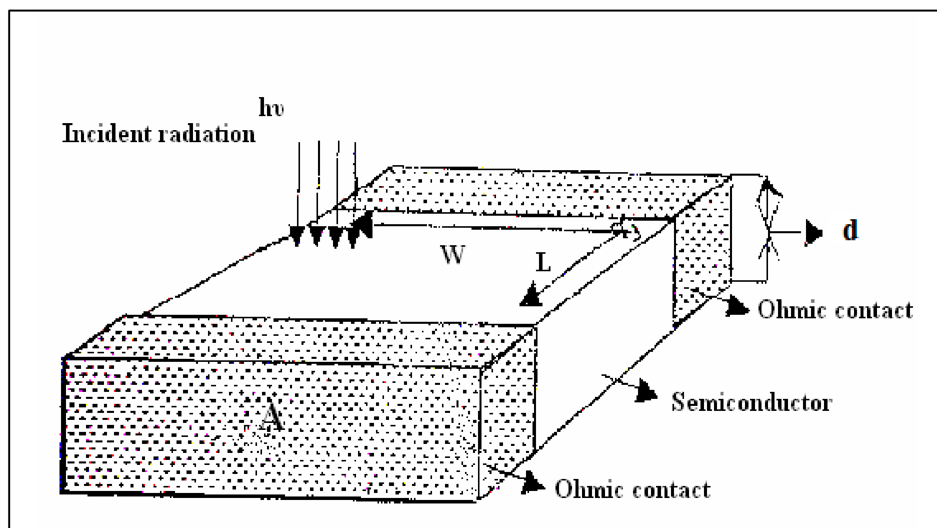

Fig.2.5: Photoconductive Detector [96].

The incident photon energy creates free carriers in the crystal and changes the conductivity of the material [94]. This type of detector can be used for automatic light control in homes and office buildings to turn light on at dawn and off at dark .Also, they are useful in optical signaling systems. The electronic transitions in photoconductive devices included:

#### 2.10.1.1 The Intrinsic Photoconductive Type

It produced when the incident photons with energy are greater than or equal to the energy band gap ($h\upsilon \geq E_g$), then an electron-hole pairs will be generated, and can limit the maximum wavelength cutoff wavelength $\lambda_c$ that detectors work is giving by equation (2-8) [96,97].

#### 2.10.1. 2 The Extrinsic Photoconductive Type

Since semiconductors have states located (energy levels) either donors or acceptors in the band gap , the energy required to ionize these must be smaller than the intrinsic energy, so that the quantum energy with $h\upsilon > E_i$ , where $E_i$ activation energy for donors ($E_D$) or acceptor ($E_A$), is absorbed then transition of electron from donor level to the conduction band for n-type or, transition of holes from the valence band to acceptor levels for p-type takes place but not both. In both cases the concentration of carrier increases so that the conductivity of semiconductor will increase also. This type is called photoconductive detectors as shown in fig.2.6.The cut off wavelength $\lambda_c$is given by [98].

$$\lambda_c = \frac{1.24}{E_i(\mathrm{eV})} \qquad (2\text{-}53)$$

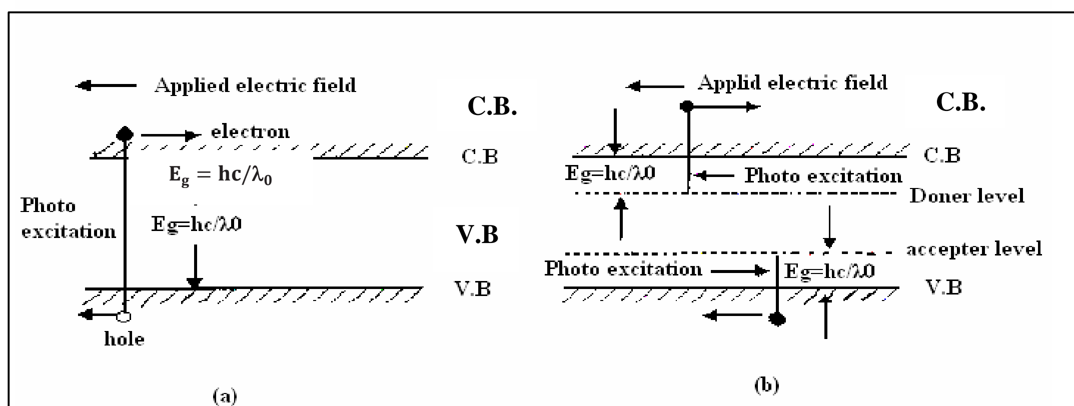

Fig.2.6: Processes of Photoconductive for Semiconductor
(a) Intrinsic, and (b) Extrinsic [99].

Other types of photoconductivity are possible which are not associated with a change in the free-carrier concentration. For example, when long-wavelength electromagnetic radiation, which does not cause interband migration and does not ionize impurity center, is absorbed by free carriers, the energy of the carriers is increased. Such an increase leads to a change in carrier mobility and, consequently, to an increase in electrical conductivity. Such secondary photoconductivity decreases at high frequencies and is not frequency dependent at low frequencies[100].

The change in mobility upon exposure to radiation may be caused not only by an increase in carrier energy but also by the effect of the radiation on electron scattering in the crystal lattice [94].

## 2.11 The Figure of Merit

There are many parameters affecting the performance of the detectors. These parameters are:

### 2.11.1 The Responsivity

Responsivity is defined as the ratio between the output electrical signals (voltage or current) to the incident radiation power or is defined as the (RMS) signal voltage to the (RMS) value of the incident radiation power. The responsivity for monochromatic light of wavelength incident normally is given by [94].

$$R_\lambda = \frac{I_{ph}}{P_{in}} \quad \text{or} \quad R_\lambda = \frac{V}{P_{in}} \qquad (2\text{-}54)$$

Where $R_\lambda$ spectral response , $I_{ph}$ photocurrent flowing between the electrodes.

### 2.11.2 The Quantum Efficiency

The quantum efficiency is defined as the efficiency with which an incident photon results in the excitation of an electron. It is a normalized value and is equal to the number of electrons excited divided by the number of photons incident on the

detector's active area. Therefore, the quantum efficiency (QE) of radiation detector is [100]:

$$QE = \frac{h\nu\, I_{ph}}{q\, P_{in}} \tag{2-55}$$

$$QE = \frac{1240\, R_{\lambda}}{\lambda_{(nm)}} \tag{2-56}$$

The quantum efficiency for an ideal detector is unity.

### 2.11.3 The Noise in Detectors

The noise is referred to the signal generated in the detector at the absence of the radiation . The relation between dark current and noise current is [99].

$$I_n = (\, 2q\, I_d\, \Delta f\,)^{1/2} \tag{2-57}$$

Where $I_n$ noise current, $I_d$ dark current, and $\Delta f$ is bandwidth.

### 2.11.4 Detectivity and Specific Detectivity

The detectivity (D) is defined as the signal-to- noise ratio per unit incident radiation power and it is defined as.

$$D = \frac{1}{NEP} = \frac{R_{\lambda}}{I_n} \tag{2-58}$$

Specific detectivity D* (normalized detectivity ) : it is the detector signal- to - noise ratio when (1) Watt of optical power is incident on the detector with optical area one $cm^2$ and the noise is measured with a band width of one Hz . It is used because it is normally dependent of the size of the detector and the bandwidth of the measurement circuit while (D) depends on both .The peak value of (D*) at specific wavelength can be written as [95].

$$D^* = D(A\Delta f)^{\frac{1}{2}} \tag{2-59}$$

Or

$$D^* = R_{\lambda}(A\Delta f)^{\frac{1}{2}} / I_n \tag{2-60}$$

The value depends on the wavelength of the signal radiation and the frequency at which it modulated.

### 2.11.5 Noise Equivalent Power

Noise equivalent power (NEP) is defined as the root mean square (RMS) incident radiant power falling on the detector that is required to produce an (RMS) signal voltage or current equal to the (RMS) noise voltage or current at the detector output it is expressed as[95]:

$$NEP = \frac{I_n}{R_\lambda} \quad (2\text{-}61)$$

The detection capability of the detector improves as the (NEP) decreases.

## 2.12 ZnO and its Dopant of Gas Sensors

ZnO is used as a semiconducting gas sensor due to its conductivity changes when exposed to oxidizing gases such as ozone. Until now, ZnO-based elements have attracted much attention as gas sensors because of their chemical sensitivity to volatile and other radical gases, their high chemical stability, suitability to doping, non-toxicity, and low cost [101].

### 2.12.1 Thin Film Sensor

Sensors have developed relatively slowly in the semiconductor device area. But, in light of increasing demand for security, environmental control, health improvement, and so on, sensors are expected to become more important and grow at a faster pace in the near future. Fig.2.7 shows that the measure is an external influence, property, or condition that is to be detected or measured by a sensor. The measured can be grouped into the following [90].

1. Thermal 2. Mechanical 3. Magnetic 4. Chemical 5. Optical

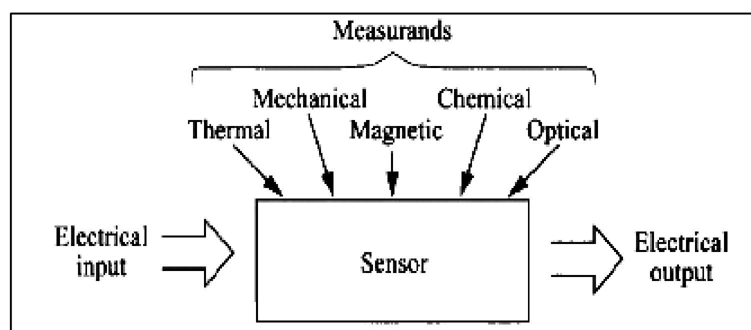


Fig.2.7: Application of a Common Semiconductor Sensor is to Monitor a Physical Quantity through the Change of Electrical Signal [90].

The range of temperature sensing depends, to the first order, on the energy gap of the materials, that is, larger $E_g$ for higher temperature. At higher temperatures or in heavily doped devices, the dopants are fully ionized, and the decrease of mobility due to phonon scattering starts to dominate the temperature dependence.

### 2.12.2 Thin Film Resistive of Gas Sensors

Resistive sensors have been used to measure a wide variety of physical and chemical properties and are among the most common and cheap sensors commercially available. For example, there are photoresistive sensors, which use materials that change conductivity with light absorption, thermoresistive sensors in which resistivity variation is controlled by the temperature, piezoresistive sensors, that use the change in resistance with mechanical stress, magnetoresistive sensors based on the resistivity change in the presence of an external magnetic field and chemoresistive that measure the resistivity change produced by the interaction of a chemical substance with the sensing material. The materials employed in these sensors are frequently produced in thin film form and in many cases can be produced by magnetron sputtering [90].

Furthermore, materials of the kind employed in these devices have been prepared for other purposes. In the gas sensor field, the most suitable materials for sensors of the chemoresistive type are metal oxides. Although the effect of the ambient atmosphere upon the electrical conductance of semiconductors was known before [102] , it was not until Seiyama and co-workers [103] that this knowledge was applied to gas detection. The first commercial gas sensor was developed by Tagushi not long after the work of Seiyama. Since then many other devices were developed and the number of materials used in gas detection has not stopped growing.

## 2.13 Sensing Properties

Sensing by metal-oxide semiconductors like ZnO is based on the oxidation–reduction reaction of the detected gases occurring on the semiconductor surface, which leads to an abrupt change in conductance of the sensor. For this reason, the

gas-sensing ability of metal oxide semiconductors is in theory very sensitive to the crystal faces of the sensing materials.

### 2.13.1 Gas and Chemical Sensing

The mechanism of sensing by the oxide thin films, is based on electrical conductance change upon surface reduction - oxidation (redox) reactions with gas species [104]. The effect of grain boundary in the polycrystalline thin film metal oxide sensors was studied and showed that it limits the repeatability and long term stability, and the crystalline structure also can be affected the sensitivity of the chemical sensor [105], the gas sensing depending on the variation of resistivity of ZnO thin film prepared by atomic layer deposition (ALD) technique was studied [106], the measured values showed that sensitivity was extremely high for ultrathin ZnO films.

### 2.13.2 Chemical Sensors

As defined previously, chemical sensors are devices used to ascertain the chemical properties of materials. This is a fast growing field of research where steadily appear new ideas and prototypes. Unlike other sensor fields, though, the number of mass-produced devices does not generally follow the research activity.

Many chemical sensor devices have large batch-to-batch irreproducibility, which originates high costs due to the need to calibrate each single device; skilled staffs are usually needed for accurate calibration and general troubleshooting and, in many cases, devices are not even suited for mass production [107].

Another problem is the large number of interfering parameters that make very difficult a complete characterization of chemical sensors. Thus frequently the progress in technology surpasses science and reduces sensor optimization to a trial and error process. The basic concept of the gas and chemical sensing by metal oxides is based on the interaction of the gas or vapor with the oxygen vacancies at the surface of the sensitive layer as shown in fig.2.8.

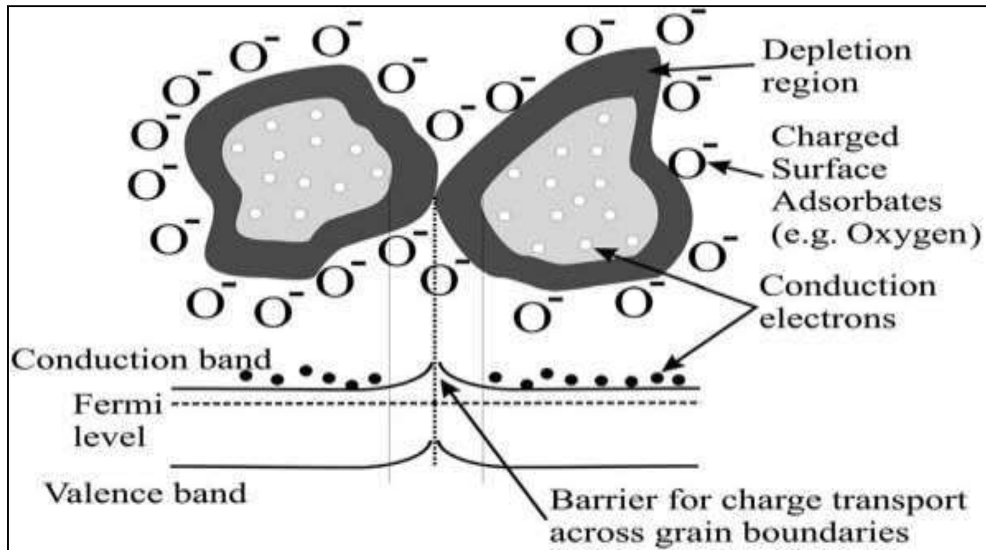


Fig.2.8. The Oxygen Vacancies at the Surface of the Grain [108].

Some metal oxides are intrinsically n-type semiconductors, the stoichiometeric excess being due to oxygen vacancies. The conductivity of the surface has revealed to be much less than that of the bulk [109]. This has been attributed to the formation of surface oxygen ions that trap electrons, inducing a surface depletion layer and thus the development of Schottky barriers at interparticle contacts. The surface barrier height $\emptyset_s$ is given by:

$$\emptyset_s = \frac{e(N_s\theta')^2}{2\varepsilon_r N_D} \qquad (2\text{-}62)$$

Where $N_s$ is the number of the surface states, $\theta'$ is the fractional occupancy, $N_D$ is the number of donor states per unit volume in the bulk, and $\varepsilon_r$ is the relative permittivity of the film material. In the case of n-type metal oxides, since the electrons come from ionized donors via the conduction band.

The charge carrier density at the interface is thereby reduced and a potential barrier to charge transport is developed as in fig.2.9 [110].

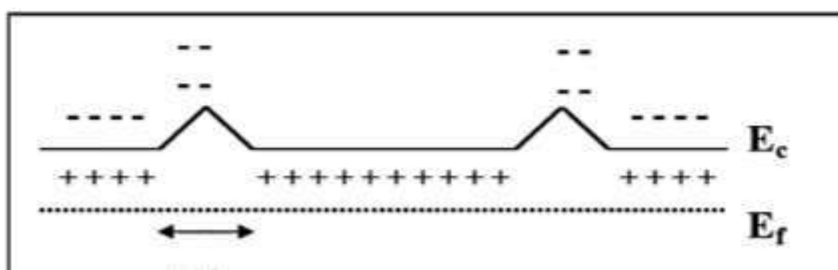

Fig.2.9: The Potential Barrier at the Interface of n-type Metal Oxide [108].

It is due to the adsorption of oxygen ions at the surface, the resistance at the junction between the grains of the solid will be changed leading to depletion layer. In the presence of a reactive gas or chemical vapor, the surface coverage of adsorbed oxygen ions might be decreased and the resistance will be decreased as a consequence of the reduction in the surface potential-barrier and depletion length, so the depletion layer width will be [109].

$$w = \frac{Q_s}{N_D e \bar{A}} \qquad (2\text{-}63)$$

Where $Q_s$ is the charge associated with oxygen surface coverage, $\bar{A}$ area of the sensor then the model expressing the surface oxygen species could be chemically formulated:

electron. ′ Where n

The presence of nanocrystallite is an important parameter for gas sensing because it offers a significant increase in surface area compared with the microcrystalline [108].

**2.14 Gas Sensing Properties**

Gas sensing materials is one of the earliest discovered and the most widely applied oxide gas sensing material. It is sensitive to many sorts of gases, and has satisfactory stability. Its gas selectivity can be improved by doping additives and catalysts.

**2.14.1 The Sensitivity**

The sensitivity of sensors is defined as the relative variation of the resistance of the sensitive thin film in percent per ppm of applied gas concentration [111].

$$(2\text{-}65)\ S_t = \left|\frac{(R_g - R_a)}{NR_a}\right| \times 100\%$$

$R_g$ are the electric resistance of the sensor in Where $S_t$ sensitivity of sensor , $R_a$ and air and in presence of gas respectively and N is the gas concentration. Although it can be calculated from conductance as in relation:

$$(2\text{-}66)\ S_t = \frac{G_{gas}}{G_{air}}$$

Where $G_{air}$ is the conductance of the sensor in pure and dry air and $G_{gas}$ is the conductance of the sensor in the air containing a given concentration of reducing gas [112].

The conductance of the sensor will be changed with the change of the resistance as in relation:

$$(2\text{-}67)\ G_{gas} = \frac{1}{R_{gas}}$$

At a given temperature, the conductance will be proportional to the gas pressure as:

$$(2\text{-}68)\ G_{gas} \cong (P_{gas})^y$$

Where $(P_{gas})$ is the partial pressure of the reducing gas in the air and y is the characteristic exponent, lower than one , depending on the kind of gas and composition of gas sensitive layer. The oxygen adsorbed on the sensor surface, then when the air contains so-called reactive gases or vapors, the reaction in the combustion of these gases depends on the adsorbed oxygen. The free electrons caused by oxygen vacancies may be assumed to cross the Schottky barriers that appear during the oxygen chemisorption by thermoionic emission [112].

$$(2\text{-}69)\ G_{air} = G_O \exp\left(\frac{-eV_{air}}{K_B T}\right)$$

$$(2\text{-}70)\ G_{gas} = G_O \exp\left(\frac{-eV_{gas}}{K_B T}\right)$$

1)٧ $$(2\text{-}\ S_t = \frac{G_{gas}}{G_{air}} = \exp\left(\frac{eV_{air} - eV_{gas}}{K_B T}\right)$$

Where $eV_{air}$ and $eV_{gas}$ are the Schottky barrier between grains in air and gas respectively.

2)٧ $$G \cong \exp\left(\frac{-eV_s}{KT}\right)^x \quad (2\text{-}$$

Where x is a specific exponent. The sensitivity depends on the gas concentration.

### 2.14.2 The Selectivity

This characteristic is related to the discrimination capacity of semiconductor gas sensor (SGS) device in front of a mixture of gases. As it is well known, we can obtain almost the same conductivity value for different gas species and concentrations. One of the possible solutions to this problem would be the mathematical treatment of every sensor signal and the different responses of a sensor array [113]. On the other hand, we could also change the sensor transducer function, introducing electronic elements to our integrated devices [114].

Both possibilities wouldn't modify our sensing material, but would increase the complexity of devices. Thus, in order to simplify the device implementation it is interesting to modify material characteristics for example by introducing catalytic additives, which can enhance the material activity toward determinate gas species and reduce it for the rest [115].

## 3.1 Introduction

This chapter focuses on the experimental details used in fabrication and investigation of pure ZnO, and $Mg_xZnO_{1-x}$ thin film with different mixing concentrations (0,30, 50 ,70, and 90) %. by chemical spray pyrolysis on glass and silicon substrates with keep deposition condition. The techniques used for preparation

and testing the structure of the thin films are the investigation about of the X-ray diffraction (XRD), morphological features by atomic force microscopy (AFM), field emission scanning electron microscope (FESEM) and determination of grain size. The Raman shift measurements by Raman spectroscopy of the films. The optical measurements by UV-Vis spectra of the thin films are presented. The electrical properties of the thin films such as D.C electrical conductivity, and Hall effect. Also study gas sensor the setting measurements of the sensing (chemical) is the final part of this chapter. A schematic diagram illustrates of the experimental work is shown in fig.3.1. The chemical materials used in this work are listed in table 3.1.

Table 3.1: Chemical Materials that Used in the Preparation.

| No. | Chemical Materials | Manufacturer | Purity % |
|---|---|---|---|
| 1 | Magnesium Acetate | China | 99.2 |
| 2 | n -Zinc Acetate | China | 99.9 |
| 3 | Nitrogen | United Arab Emirates | 99.9 |
| 4 | HF-Solution | Aldrich | 99.2 |
| 5 | Ethanol | Bio solve | 99.9 |
| 6 | Conductive Silver Paste | China | 99.0 |
| 7 | n-Silicon Wafer (111) | USA | 99.0 |
| 8 | n-Silicon Wafer (100) | USA | 99.0 |

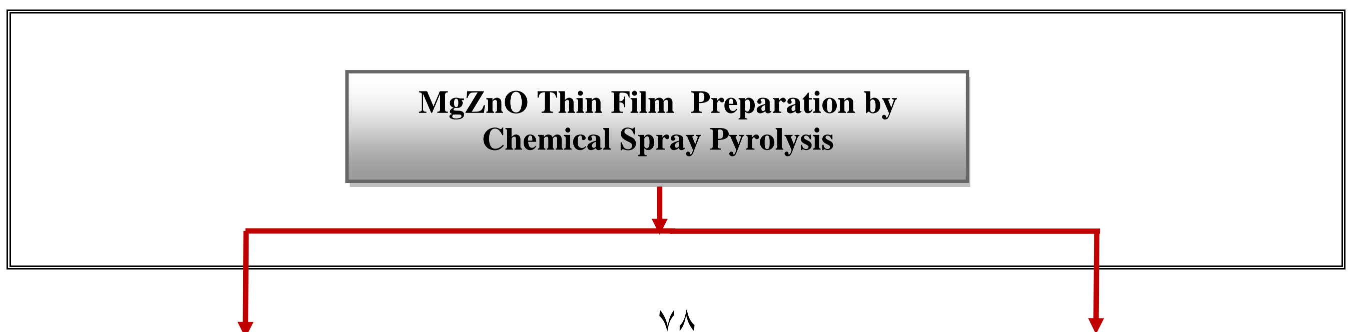

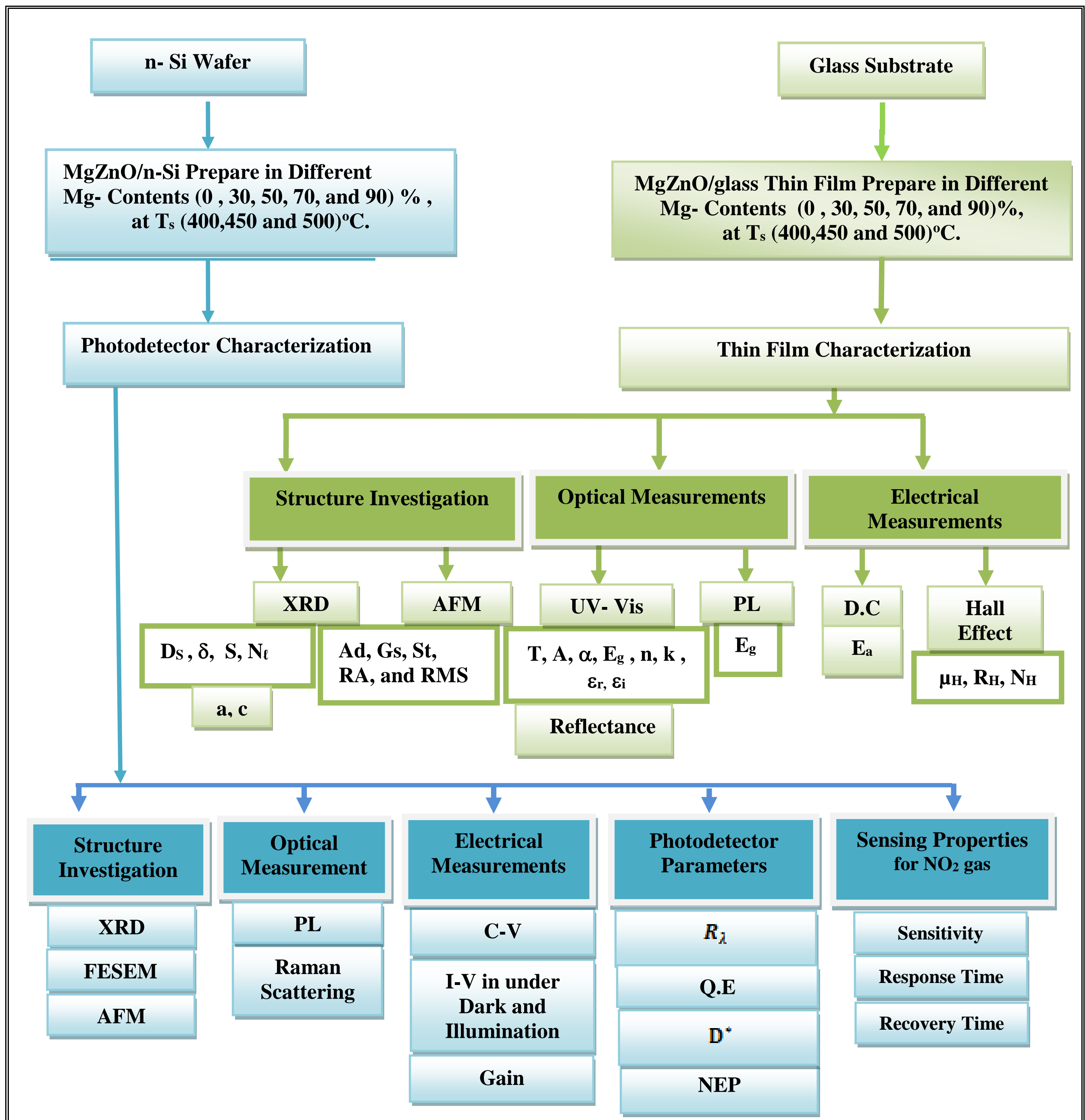


Fig.3.1: Schematic Diagram of the Experimental Work

## 3.2 Preparation of $Mg_xZnO_{1-x}$ Thin Film

The chemical spray pyrolysis (CSP) technique has been used for preparing the $Mg_xZnO_{1-x}$ thin film on substrate temperatures (400,450, and 500) °C and deposition $Mg_xZnO_{1-x}$ on the glass and silicon substrates.

### 3.2.1 Experimental Set-up of (CSP)

The $Mg_xZnO_{1-x}$ thin film were deposited on a glass substrate by using (CSP) homemade equipment as illustrated in fig.3.2.

The (CSP) equipment consists of the precursor solution in the atomizer (with timer) by the way of a carrier gas pumped from a gas cylinder (Nitrogen) at controlled pressure by a system of pressure gauges, substrates heater, and temperature controller.

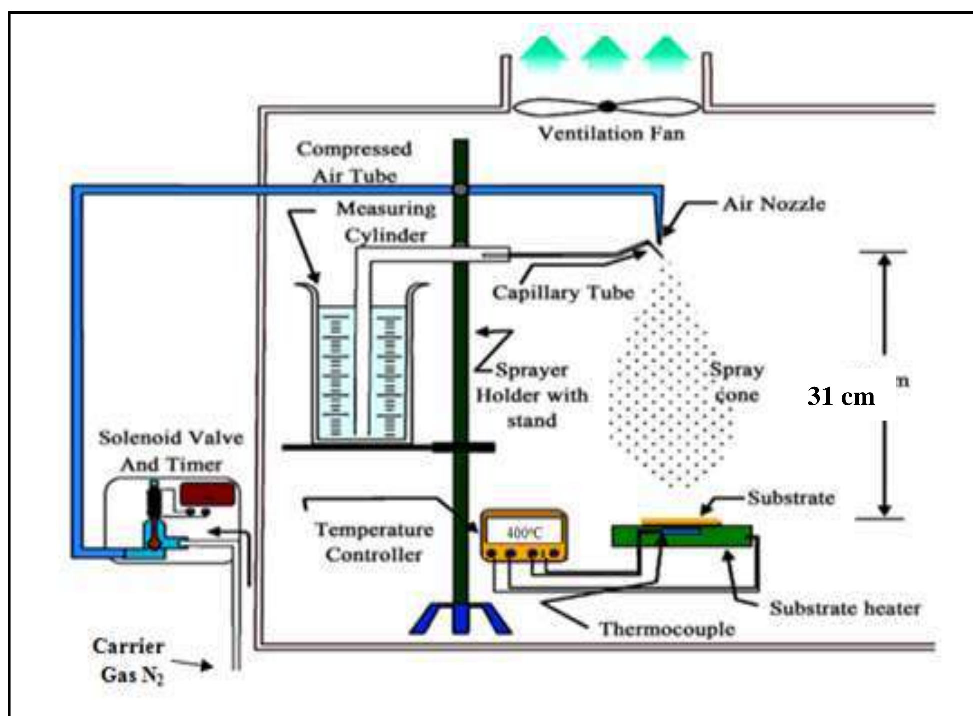


Fig.3.2: Schematic of Spray Pyrolysis Equipment.

Thin film deposition using (CSP) can be divided into three main steps: atomization of the precursor solution, transportation of the resultant aerosol, and decomposition of the precursor on the substrate. In this work will be applied the optimum condition on (CSP) system to get the thin films homogeneity. Temperature has significant effect upon the homogeneity of the prepared films, because it is responsible for the varying of crystal structure of material that affects physical properties of materials. The preparation temperatures of thin films were different (400,450, and 500) °C. To obtain a homogenous film, the spraying rate must be kept constant during deposition. That is because this parameter affects the homogeneity

and thickness of the prepared films. Sprayer operation should be uniform, so it is important to control the time period between every spraying. Moreover it should be constant. The spraying time period was (9) s with (90) s wait between the steps of spraying spatters number were 20 sprays, and spray rate is 10 mol / min. In our study the best height for the nozzle spray was (31) cm, any excess in this distance cause scattering for the atomized solution away from the substrate, also any decrease in the distance will cause the collection of solution drops in one spot and this will affect film homogeneity. The carrier gas was (compressed nitrogen) and the solution is fed into a sprayer nozzle at a pre-adjusted constant atomization pressure (4.5) bar to get uniform films. In this work preparing thin films in kept thickness, from during are kept number of spray.

**3.2.2 Preparing of Substrates**

The cleaning of substrates is very important process because the influences like oil or dust effect on the properties of thin films, clean substrate is also essential to achieve good film adhesion.

**3.2.2.1 Glass Substrate**

ZnO and MgO thin films deposited on glass substrate, made in China , have dimension (2.5×2.5) $cm^2$ area using a steel-cut machine. The cleaning of substrates is very important process because the influences like oil or dust effect on the properties of thin films. This process can be summarized in the following steps:

1. Washing the glass substrate with water and cleaning powder to remove any oil or dust that might be on the substrate of the surface, then putting them under tap water for (15) min.
2. Placing the glass substrates in a clean beaker containing distilled water and then rinse in ultrasonic waves for (15) min. Immersing the glass substrates in a beaker containing a pure alcohol solution with purity (99.9)% which reacts with contamination such as oil and dust that might be on the substrate of the surface. Put the beaker in the ultrasonic waves for (15) min.

3. Finally, drying the substrates and with soft paper (lines paper) and kept to be used in time. Now the slides are ready to deposit the thin films on them.

#### 3.2.2.2 Silicon Substrate

Si-wafer was n-type (111) with resistivity about (1.5- 5) Ω cm and (500±10) µm thickness. Square-shaped n-type silicon samples, each of (1.5×1.5) $cm^2$ area were prepared using a steel-cut machine. Silicon wafers were washed ultrasonically in distilled water and were immersed in ethanol with a purity of (99.9)% in order to remove dirt and oil, while native oxide layer removed by etching in dilute (2:10) HF: $H_2O$ for (3) min. the silicon wafers were cleaned in distilled water and dried in furnace at (100) °C.

### 3.2.3 Preparation of the Spray Solutions

Films of $Mg_xZnO_{1-x}$ with different Mg-contents were deposited on a glass substrate by chemical spray pyrolysis (CSP) technique under ambient atmosphere.

Two kinds of aqueous solutions, Zinc acetate $Zn(CH_3COO)_2.2H_2O$ of (99.9)% purity and molecular weight equal to (219.52) g/mol and Mg acetate $Mg(CH_3COO)_2.4H_2O$ of (99.2)% purity and molecular weight equal to (214.46) g/mol, were chosen as the sources of Zinc and magnesium respectively. The weights of $Zn(CH_3COO)_2.2H_2O$ and $Mg(CH_3COO)_2.4H_2O$ were measured by using electrical balance sensitive (Metller. A.K -160 ) four digits $10^{-4}$ g.

In order to obtain $Mg_xZnO_{1-x}$ thin film with different Mg-contents (x = 0,30, 50, 70, and 90)%, the deposition parameters were the same for the series of $Mg_xZnO_{1-x}$ thin film. The pure Zinc acetate , pure Magnesium acetate, and distilled water were mixed thoroughly to get the solution with a concentration of (0.1) M and a few drops of glacial acetic acid were then added to stabilize the solution were added to (100) mL solution to increase the solubility of the compounds. The substrate temperatures were (400,450, and 500) °C during the films growth. The solution was stirred for (30)min. with a magnetic stirrer.

### 3.2.4 Masks and Ohmic Contact

Aluminum sheets are used in order to make the masks to get the desired shape of electrodes as shown in fig.3.3. Shows all kinds of masks there were used in the evaporation steps. The masks have the same size of the substrate were exactly attached and fixed over the substrate after being cleaned that achieved as follows:

1. The masks are placed in ethanol for 10 min.
2. The masks are washed by distilled water.
3. They have immersed in pure alcohol for 5 min.
4. Dried with blowing air.

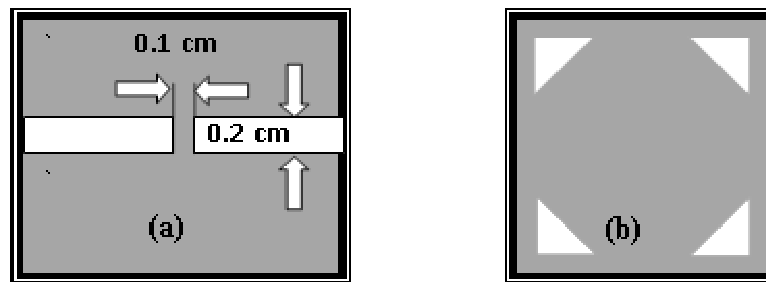


Fig.3.3: The Masks Used for (a) (D.C) Measurement (b) Hall Effect

Ohmic contacts for the prepared films are produced by evaporating (Al) electrodes by means of thermal evaporation method using Edward's type (E306A) unit.

## 3.3 Structural and Morphological Measurements

The structure properties shown below:

### 3.3.1 X-Ray Diffraction

The crystal structure and crystallinity of as-grown $Mg_xZnO_{1-x}$ thin film such as nanocrystallite size, structure aspect layer and lattice constant have been investigated by X-ray diffraction (XRD) using SHIMADZU X-ray diffractometer system (XRD-6000) which record the intensity as a function of Bragg's angle. The sample is scanned from (20-60) degree. The conditions of the system were:

- Source $CuK_\alpha$ with radiation of wavelength $\lambda = (1.54)$ Å.
- Target: Cu
- Current emission = (30) mA.
- Applied voltage = (40) KV.

- Scanning speed = (5 ) deg./min.

### 3.3.2 Field Emission Scanning Electron Microscopy

The morphological properties of the $Mg_xZnO_{1-x}$/n-Si photodetector were investigated by (FESEM) and energy-dispersive X-ray spectroscopy (EDX). The (FESEM) is type (S-4300 of Hitachi, S-4700 FESEM) in Islamic Republic of Iran/ University of Tehran / Razi foundation. The FESEM is used in its common mode, the field mode and the emission mode. In this mode, electrons fired from the electronic gun are accelerated with a voltage (15) KV, which consisting of two magnetic lenses. The main aim of these lenses is to focus a fine electron beam onto the sample. Scanning coils placed before the final lens causes the electron spot to scan across the sample surface in the form of a square raster.

The current that passes through these coils which are typically made to pass through the deflection coils of the cathode ray tube and regenerated on a computer screen to generate the image. There is an interaction between the atoms and electrons in the sample. This interaction causes various signals to generated and the most commonly used signals are those from secondary back-scattered electrons. The secondary electrons are electrons of very low energy and thus, contain information of only a few angstroms deep on the surface of the layer. These electrons are then detected by a detector consisting of a scintillator -photomultiplier combination, which in turn through the system electronics drive the cathode ray tube. These images are the ones commonly used in FESEM to interpret the morphology of a sample.

### 3.3.3 Atomic Force Microscopy

The operation principle of an AFM is presented in fig. 3.4 the AFM, consists of a cantilever and a sharp tip at its end. The surface of the sample is scanned with the tip. The distance between the sample surface and the tip is short enough, to allow the Van der Waals forces between them to cause deflection of the cantilever. The deflection follows Hooke's law and the spring constant of the cantilever is known, thus the amount of deflection and further, the topographical profile of the sample, can be determined. AFM micrographs were taken with a digital instruments, Inc.

Nanoscope III and dimension 3100**.** Typical data has been taken from AFM height images which include root mean square (RMS) roughness and grain size. It has three main modes of mapping topography: contact ,non-contact which is used in our morphology investigation and intermittent contact or tapping. The most important part of an AFM is the tip with its nanoscale radius of curvature. This device is present in the University of Baghdad / College of Science / Department of Chemistry.

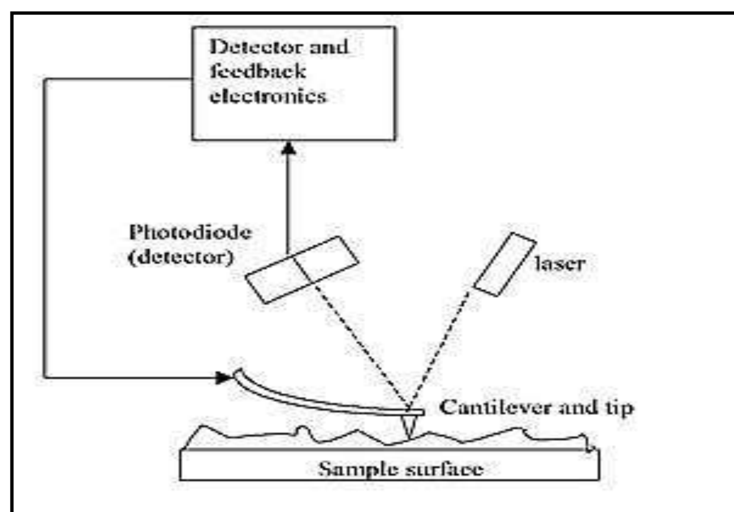


Fig.3.4:The Operation Principle of AFM.

### 3.3.4 Raman Shift Measurements

The Raman scattering spectroscopy (RSS) measurements for the thin film $Mg_xZnO_{1-x}$ /n-Si photodetector were investigated by (RSS) in Islamic Republic of Iran / University of Saniti Sharif / Sharif spectroscopy laboratory. Raman spectroscopy is a spectroscopic technique based on inelastic scattering of monochromatic light, usually from a laser source. Inelastic scattering means that the frequency of photons in monochromatic light changes upon interaction with a sample. Photons of the laser light are absorbed by the sample . Frequency of the photons is shifted up or down in comparison with original monochromatic frequency, which is called the Raman effect.

This shift provides information about vibrational, rotational and other low frequency transitions in molecules. Raman spectroscopy can be used to study solid, liquid and gaseous samples.

### 3.3.5 Film Thickness Measurements

Thickness is one of the most important parameters of thin film because it largely determines the properties of the film. There are several methods used for measuring the thickness of thin film. Form this fact a great diversity in methods of thickness measurement follows. In our work the thickness of the films were measured by using two types:

- Reflectance measurements:

The film thickness was estimated with (Spectroscopic reflectometer and film thickness measurement system, (SR300), angstrom sun technologies Inc. USA).

- The weight method:

This method is done by using sensitive electrical balance of type (AE 166 Metter). This method gives an approximate deposited film thickness and can be summarized as follows: The substrates are weighted before and after deposition and the variation in weight of substrate represent the thin film dimensions.

## 3.4 Optical Properties Measurements

The optical measurements are achieved on prepared thin films including: Transmittance, absorbance and reflectivity.

### 3.4.1 UV-Vis Measurements

The optical properties were examined via (CARY100 CONC plus UV-Vis-NIR, Split- beam Optics, Dual Detectors) spectrophotometer equipped with a xenon lamp at a wavelength range at (300-700) nm. All thin films were deposited on glass substrates. The band gap of the prepared material with sharp fall off can be deduced from a plot of the squared absorption coefficient $(\alpha h\upsilon)^2$ versus photon energy (hυ) by extrapolating the straight line of the plot to intersect the energy axis. This device is present in the University of Kufa / College of Engineering / Unite of Nanotechnology.

### 3.4.2 Photoluminescence Measurements

Photoluminescence (PL) is an important physical phenomena used to characterize semiconductors it depicts samples energy structure to reveal other important material features.

The transition energy of the samples is measured using (Scinco,FS-2, Fluorescence Spectrometer-Meter, Xenon Lamp Power Supply).

## 3.5 Electrical Measurements

The electrical measurements are achieved on prepared thin films including, D.C conductivity and Hall effect.

### 3.5.1 The Direct Continuous Conductivity Measurements

The D.C conductivity measurement of $Mg_xZnO_{1-x}$ thin film deposited on glass substrate at different temperatures (400,450, and 500) $^oC$, with (Al) electrodes could be calculated by measuring the electrical resistance as a function of temperature in the range (300-443) K using sensitive digital electrometer type Keithly model 2400, and electrical oven (Memmert Lab. Oven UFB 400,400W).

### 3.5.2 Hall Effect Measurements

Hall effect system (Ecola, Hall effect measurement system, HMS-3000) was used in the present study. Hall measurement is widely used in the initial characterization of semiconductor to determine the following characteristics: electrical resistivity($\rho$), electrical conductivity($\sigma$), carrier mobility ($\mu$), Hall coefficient ($R_H$), carrier concentration (n), and type carrier (n or p).

### 3.5.3 The Photodetector Al/ $Mg_xZnO_{1-x}$/n-Si/Al Characterization

The electrical properties of photodetector were studied. All measurements were carried out under dark room and illumination. The electrical measurements involved capacitance - voltage and current -voltage measurements.

#### 3.5.3.1 Capacitance -Voltage Measurements

Capacitance measurements as a function of reverse voltage (C-V) for Al/$M_xgZnO_{1-x}$/n-Si/Al photodetector were carried out using (LCR) meter at a frequency of (0.6-1) MHz.

The charge-carrier density and width of the depletion layer for device are calculated by using the equation (2-39).

#### 3.5.3.2 Dark and Illumination for Current-Voltage Measurements

The dark and illumination current as a function of forward and reverse bias voltage in the range {(-1) to (1)}V for all prepared $Mg_xZnO_{1-x}$/n-Si photodetector with various deposition conditions was carried out using Keithley digital electrometer type (616) model 2400 and d.c power supply. From the plot of the forward current ($I_a$) versus applied forward bias voltage ($V_a$), the ideality factor (η) was obtained according to the relation (2-43). The value of the constant (γ) was also measured according to the relation (2-46). The characteristics (I-V) illuminated with reverse bias voltages with various deposition conditions were performed with intensities (60) mW/cm2 (measured by solar meter).

### 3.6 Figure of Merit of $Mg_xZnO_{1-x}$ /n-Si Photodetector

Photocurrent is one of the most important parameter in the spectral responsivety ($R_\lambda$), quantum efficiency (Q.E), specific detectivity ($D^*$), and noise equivalent power (NEP). Spectral resopnsivity of $Mg_xZnO_{1-x}$ /n-Si photodetector was measured by using the system which is consisted of monochrometer in the range (400-1100) nm, electrometer and power meter for measuring the radiation power for each wavelength and d.c power supply to supply bias voltage on each side of the detector this was measured in the University of Technology/ Department of Applied Science . From the ($R_\lambda$), (Q.E), (D*), (NEP), and detectivity (D), were obtained using equations {(2-54) - (2-61)} respectively.

### 3.7 Gas Sensor System

In order to determine the sensitivity parameter mainly the response time and recovery time of the fabricated $Mg_xZnO_{1-x}$ /n-Si, suitable setup is prepared for this purpose. Fig.3.5 shows the gas sensor testing system, which it consists of, cylindrical stainless steel test chamber of (30) cm diameter and (35)cm height. It has an inlet for allowing the tested gas to flow in and an air admittance valve to allow the flow of atmospheric air after evacuation. A multi pin feedthrough at the base of the chamber allows the electrical connections to be established to the heater, K-type thermocouple, and sensor electrodes. The heater consists of a hot plate and a K-type thermocouple inside the chamber in order to control the operating temperature of the sensor as

shown in the fig.3.5. PC-interfaced digital multimater of type (UNI-T UT81B) , and Laptop PC, is used to register the variation of the sensor current when exposed to (air-$NO_2$) gas mixing ratio. The mixing gas is fed by zero air and test gas through a flow meter and needle valve arrangement. The mixing gas is feeding through a tube over the sensor inside the test chamber to give the real sensitivity.

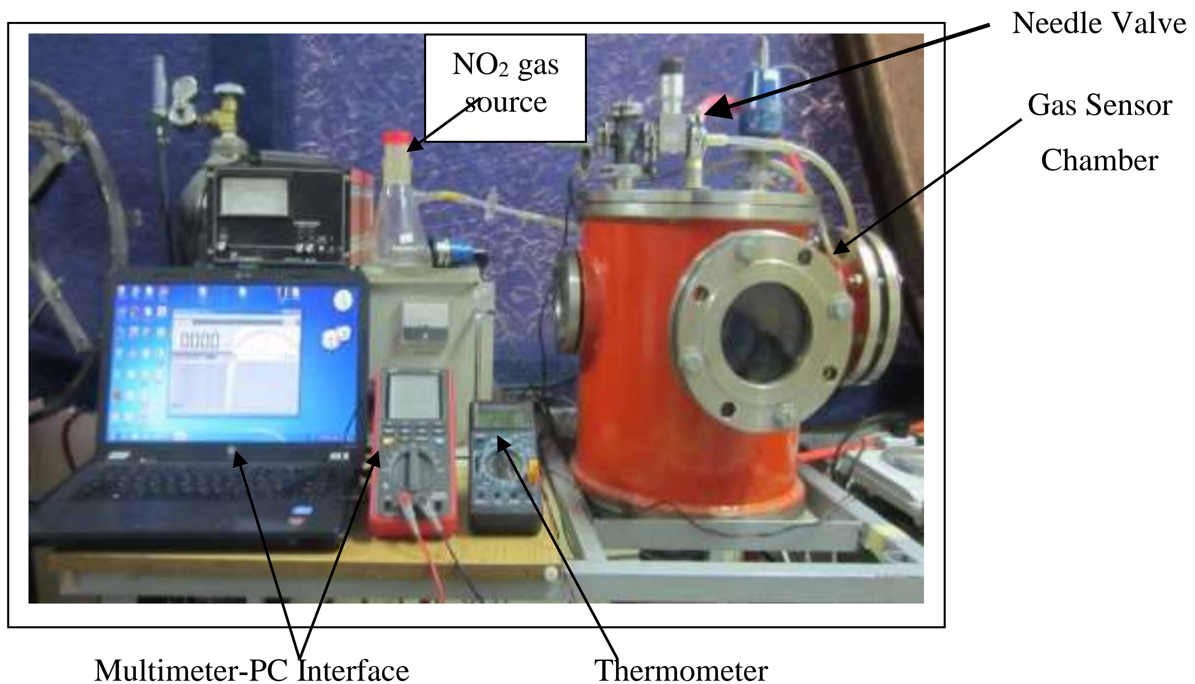


Fig. 3.5: Image of Gas Sensor Testing System

### 3.8 Al-Interdigitated Electrodes

In order to fabricate the gas sensor, a special mask needs to be fixed carefully on the surface of $Mg_xZnO_{1-x}$/n-Si layer. Interdigitated aluminum Ohmic metal contacts are deposited on the $Mg_xZnO_{1-x}$/n-Si photodetector by using vacuum evaporation technique. figs. (3.6 and 3.7) show the schematic diagram of interdigital electrodes of the $Mg_xZnO_{1-x}$/n-Si gas sensor, in which the part of blue and white are $Mg_xZnO_{1-x}$ /n-Si photodetector and electrodes, respectively.

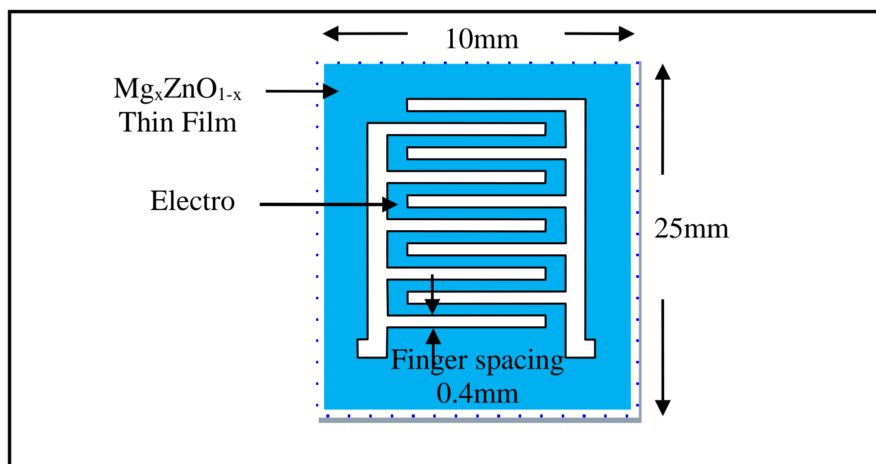


Fig.3.6:Schematic Diagram of Interdigital Electrodes.

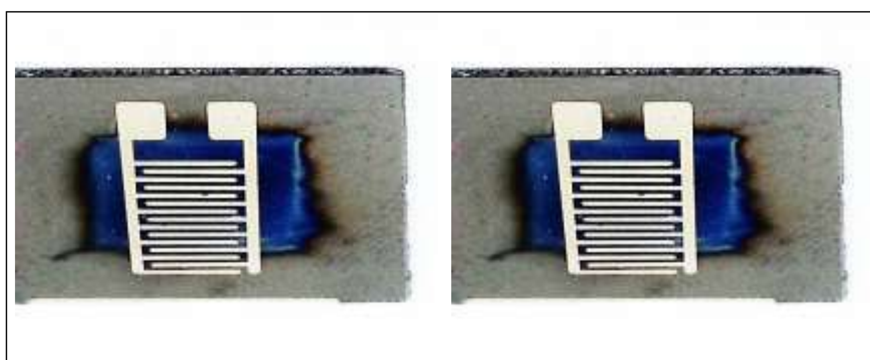

Fig.3.7: Photographic Plate of Photoconductive Mask, and Samples of ZnO/n-Si Gas Sensor and $Mg_xZnO_{1-x}$/n-Si Gas Sensor.

### 3.9 Sensor Testing Procedure

The operation of the test setup is illustrated in the following points:

1. The test chamber is opened and the sensor placed on the heater. The necessary electrical connections between the pin feed through and the sensor was done using conductive aluminum sheet, and the test chamber is closed.
2. A bias voltage of 6V between the two sides of the electrodes is applied.
3. Switch on the rotary pump to evacuate the test chamber to (1)mbar, and setting sensor to desired operating temperature using temperature controller. Fig.3.8 illustrated the schematic diagram of the electrical circuit for gas sensing measurements.